AD-A114 018 CAMBRIDGE UNIV (ENGLAND) CAVENDISH LAB F/G 17/5
LIQUID IMPACT EROSION MECHANISMS IN TRANSPARENT MATERIALS.(U)
MAR 82 S V ZWAAG, J E FIELD AFOSR-78-3705
UNCLASSIFIED AFWAL-TR-82-4022 NL

1 OF 1
AD A
114018

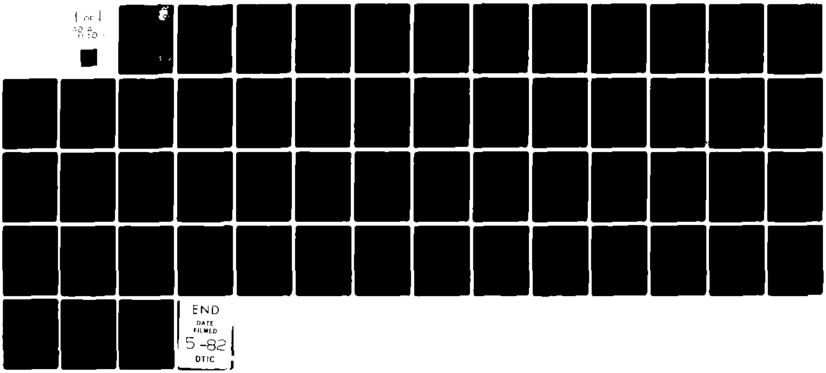

END
DATE
FILMED
5-82
DTIC

AFWAL-TR-82-4022

LIQUID IMPACT EROSION MECHANISMS IN TRANSPARENT MATERIALS

Dr. S. van der Zwaag
Dr. J.E. Field

Physics and Chemistry of Solids
Cavendish Laboratory
Madingley Road
Cambridge CB3 OHE UK

March 1982

Interim Report for Period: 30th September 1980 - 30th September 1981

Approved for Public Release: Distribution Unlimited

DTIC
ELECTE
S APR 30 1982 D
D

MATERIALS LABORATORY
AIR FORCE WRIGHT AERONAUTICAL LABORATORIES
AIR FORCE SYSTEMS COMMAND
WRIGHT-PATTERSON AIR FORCE BASE, OHIO 45433

NOTICE

This report has been reviewed by the Office of Public Affairs (ASD/PA) and is releasable to the National Technical Information Service (NTIS). At NTIS, it will be available to the general public, including foreign nations.

This technical report has been reviewed and is approved for publication.

G F Schmitt

G. F. SCHMITT, Project Engineer
Coatings and Thermal Protective Materials
Branch
Nonmetallic Materials Division

William C Kessler

W. C. KESSLER, Chief
Coatings and Thermal Protective Materials
Branch
Nonmetallic Materials Division

FOR THE COMMANDER

F D Cherry

F. D. CHERRY, Chief
Nonmetallic Materials Division

"If your address has changed, if you wish to be removed from our mailing list, or if the addressee is no longer employed by your organization please notify AFWAL/MLBE, W-PAFB, OH 45433 to help us maintain a current mailing list".

AIR FORCE/56780/19 April 1982 — 260

REPORT DOCUMENTATION PAGE

READ INSTRUCTIONS BEFORE COMPLETING FORM

1. REPORT NUMBER AFWAL-TR-82-4022	2. GOVT ACCESSION NO. AD-A114 018	3. RECIPIENT'S CATALOG NUMBER
4. TITLE (and Subtitle) Liquid Impact Erosion Mechanisms in Transparent Materials		5. TYPE OF REPORT & PERIOD COVERED Interim Report 30th Sept.1980-30th Sept.198
		6. PERFORMING ORG. REPORT NUMBER AFOSR-78-3705C
7. AUTHOR(s) S. van der Zwaag and J.E. Field		8. CONTRACT OR GRANT NUMBER(s)
9. PERFORMING ORGANIZATION NAME AND ADDRESS Physics and Chemistry of Solids Cavendish Laboratory Madingley Road, Cambridge, CB3 OHE, UK		10. PROGRAM ELEMENT, PROJECT, TASK AREA & WORK UNIT NUMBERS P.E. 62102F, Project 2422 Task 242201, WON 24220123
11. CONTROLLING OFFICE NAME AND ADDRESS AFOSR(PKN) Bolling AFB DC 20332		12. REPORT DATE March 1982
		13. NUMBER OF PAGES 48
14. MONITORING AGENCY NAME & ADDRESS(if different from Controlling Office) Materials Laboratory (AFWAL/MLBE) Wright-Patterson AFB OH 45433		15. SECURITY CLASS. (of this report) UNCLASSIFIED
		15a. DECLASSIFICATION/DOWNGRADING SCHEDULE

16. DISTRIBUTION STATEMENT (of this Report)

Approved for public release; distribution unlimited

17. DISTRIBUTION STATEMENT (of the abstract entered in Block 20, if different from Report)

18. SUPPLEMENTARY NOTES

19. KEY WORDS (Continue on reverse side if necessary and identify by block number)

Liquid Impact, Erosion, Fracture, Zinc Sulphide, Glasses, Finite Element Analyses, Hard Coatings.

20. ABSTRACT (Continue on reverse side if necessary and identify by block number)

This project has been concerned with developing techniques for the study of liquid impact, with studying the behaviour of various infra-red transparent solids and with analytic work on hard coatings. Damage has been assessed quantitatively by measuring the "residual" strength after impact and plotting strength against velocity. Section 2 of this report describes an analysis of residual strength curves. The comparison between the analytic predictions and the experimental curves is good. Sections 3 and 4 describe the results of finite element analysis for the case of (i) Hertzian and (ii) uniform pressure loading

20. of substrates with a hard coating. The protection offered by the coating is examined in terms of the elastic properties of the coating and its thickness.

PREFACE

This report summarizes research performed at the Cavendish Laboratory, University of Cambridge, Cambridge, England from September 1980 through September 1981 under AFOSR Grant 78-3705B. The work was funded with Project 2422 "Protective Coatings and Materials," Task No. 242201 "Coatings for Aircraft and Spacecraft." The report was submitted in January 1982.

TABLE OF CONTENTS

LIST OF ILLUSTRATIONS

SECTION I

INTRODUCTION

The research on this project has been concerned with developing techniques for the study of liquid impact, with assessing the behaviour of various infrared transparent solids and most recently with analytic and experimental work on hard coatings.

As discussed in detail in our previous interim reports (1,2), we use three different techniques for studies of high velocity liquid/solid impact. The first involves projecting specimens of up to 25.4 mm diameter at stationary drops. The second fires a liquid jet at a stationary target. The third uses two-dimensional configurations (discs, wedges of liquid) which are impacted. The first approach is nearest to the practical situation in liquid impact, the second has distinct advantages in its ease of operation, low construction cost and the velocity range which can be covered. The final approach, using the two-dimensional configuration, allows processes occurring <u>inside</u> the impacted liquid to be followed by high-speed photography, and is nearer situations which can be theoretically analyzed(3,4).

In order to assess impact damage quantitatively, we measure 'residual strengths'. This involves impacting a specimen under known conditions and then measuring the strength. A hydraulic apparatus, which stresses 2" (ca. 51 mm) diameter disc specimens, was developed for this (5). The technique has subsequently been modified and improved (6). The technique can be used for a range of disc sizes; recently we have designed an apparatus for stressing discs of 1" (25.4 mm) diameter. This is proving useful where the amount of specimen material is limited or expensive.

Our earlier work has shown that it is possible to relate drop and jet impact in a useful manner, and to use the concept of an 'equivalent drop size' for jet impacts. Our high-speed camera work (1) showed that our apparatus produces jets which are coherent and with smooth, curved front faces. Further, since the high pressures of liquid impact occur in the first instant of impact, jet and drop impact can be made 'equivalent' to a reasonable approximation.

The present report starts by describing an analysis of 'residual' strength curves. It is shown that it is possible to correlate the various regions of the curves with the response of flaws in the material to the impact stresses. The analysis predicts the shape of the experimental curves very satisfactorily. Examples are given of the effect on changes in the flaw size distribution and changes in K_{IC} on the material response to liquid impact

Many of the materials which have attractive IR transmission properties are mechanically weak. Much of our recent research effort has been concerned with assessing the possibly beneficial effects of a thin of hard coating. Sections 3 and 4 describe the results of finite element analyses for the cases of (i) Hertzian (ii) uniform pressure loading of substrates with a hard coating. Variables are the elastic properties of the coating and its thickness.

SECTION II

LIQUID IMPACT DAMAGE IN BRITTLE SOLIDS

1. INTRODUCTION

In a previous report (2) we have described the damage in soda-lime glass due to single and multiple jet impact. The damage was quantified by measuring the post-impact strength of specimens using a specially designed hydraulic bursting technique (5,6). A typical 'residual strength' curve for single impact on a brittle material is shown in Figure 1. Three stages can be distinguished in this curve:

i) at low impact velocities no damage can be detected and the fracture stress of the specimen is as that of unimpacted specimens.

ii) at moderate impact velocities the average fracture stress decreases rapidly with increasing impact velocity. In this region there is a bimodal distribution in the results: some specimens have a low fracture stress while others, impacted at the same velocity, fail at stresses comparable to those for unimpacted specimens. The percentage of specimens with low fracture stresses increases continually with impact velocity as is illustrated in the failure probability curve shown in Figure 2. It should be emphasized that earlier work by Rickerby (7) using high-speed photography has shown that the variability in the results is not caused by jet instabilities but is due to local variations in the surface flaw size population. This explanation is supported by a new theoretical analysis of the impact damage which is described later in this section.

iii) at high impact velocities the average fracture stress still decreases continually with impact velocity but at a much lower rate. All specimens show extensive damage.

It has been shown by Bowden and Field (8) that the jet/drop impact damage in brittle materials is due to the interaction of the Rayleigh surface waves with pre-existing surface defects and the ensuing extension thereof. In the previous report (2) we have calculated the growth of surface flaws due to stress pulses simulating the Rayleigh wave generated by the impact as a first attempt to calculate the velocity dependence of jet/drop impact damage.

In this report we have extended and improved the previous model significantly by taking into account the statistical nature of the flaws in brittle materials.

2. A MODEL FOR LIQUID IMPACT DAMAGE

We now consider in some detail the various parameters which determine the impact stresses and the resulting damage and combine them to give a simple quantitative model for liquid impact damage.

a. Stress Wave Intensity

Swain and Hagan (9) have attempted to measure the magnitude and time dependence of the Rayleigh surface wave produced by an impacting jet using piezo-electric crystals. They were unable to determine the absolute magnitude of the pulse, but showed that the Rayleigh wave can be approximated, to a reasonable accuracy, by a triangular pulse. As a first approximation they used the following expression for the amplitude of the Rayleigh wave

$$\sigma_{max} = \alpha \, Z \, V_i \qquad (1)$$

where α is a constant, Z the acoustic impedance of the liquid and V_i the impact velocity. The above equation was derived by drawing an analogy with the case of quasi-static Hertzian contact where the maxium radial tensile stress depends linearly on the average pressure over the contact zone.

b. Dynamic Crack Growth

In the case of a dynamically loaded crack the stress intensity factor is initially a function of time (10-12). For a stationary crack the diffraction of a stress wave by a crack of finite dimensions leads to a damped oscillatory behaviour of the stress intensity factor around the quasi-static value.

The stress intensity factor for a non-stationary crack has been analysed in several studies (13-18). The equation for the stress intensity factor derived by Eshelby (14) is particularly applicable to the problem of propagating small flaws and is given by

$$K_d = m \, \sigma(\pi a)^{\frac{1}{2}}(1 - V/C_R)^{\frac{1}{2}} \, U \qquad (2)$$

where m is a geometrical constant, a the initial flaw size, V the current crack velocity, C_R the Rayleigh wave velocity and U is given by the following series

$$U = \left[1 + \frac{3}{8}\,\frac{c - a}{a} - \frac{15}{26}\left\{\frac{c - a}{a}\right\}^2 + \cdots\cdots\right] \qquad (3)$$

where c is the current crack size. Evaluation of this series shows that for $c < 20a$ U can be accurately approximated (16) to

$$U \simeq \left(1 + \frac{4}{5}\,\frac{c - a}{a}\right)^{\frac{1}{2}} \tag{4}$$

The current crack velocity in the above equation can be derived from the experimentally determined dependence of the crack velocity on the dynamical stress intensity factory (19)

$$V = V_{max}\ (1 - K_{IC}^{\ 2}/K_d^{\ 2}) \tag{5}$$

where V_{max} is the maximum crack velocity.

c. Flaw Statistics

The variability of the strength of nominally identical brittle specimens is due to a distribution in the size of the 'Griffith' flaws. Hunt and McCartney (20) have derived an expression relating the failure probability to the flaw size distribution. A simplified probability density function for the flaw dimensions has been derived by Jaytilaka and Trustrum (21) from experimental data and is given by

$$f(c) = \frac{c_o^{\,n-1}}{(n-2)!}\ c^{-n}\ e^{-c_o/c} \tag{6}$$

where c_o is the size of the most probable flaw dimension. The parameter n is related to the Weibull parameter m (22).

d. The Model

In order to calculate the residual strength curve for soda-lime glass the following procedure has been followed.

i) In a circular specimen flaw positions were generated at random. The total number of flaws per specimen was between 20 and 40.

ii) A flaw dimension was allocated to each of the flaw positions. All flaws were taken as normal to the radial vector from the centre of the specimen. The flaw size distribution used in the calculation is plotted in Figure 3. The most frequent crack dimension was taken as 12 μm; 99% of the flaws have dimensions smaller than 50 μm.

iii) The maximum flaw size in the specimen was used to calculate the pre-impact strength of this specimen.

iv) The impact was simulated by a stress pulse, i.e. the Rayleigh wave, moving radially outwards from the centre of the specimen. In order to simplify the calculations the stress pulse was taken as rectangular. The amplitude of this pulse decayed as $R^{-\frac{1}{2}}$, i.e. the same decay rate as the Rayleigh wave, when moving outwards over the specimen. The initial duration of the stress pulse was taken as 0.1 μs. The duration of the pulse was increased linearly with radial distance.

(v) At each flaw position the dynamical stress intensity factor was calculated according to equation 2. For flaws where K_{ID} exceeeded K_{IC} crack growth was calculated using an interation procedure in which the stress pulse was divided in 100 intervals of equal duration. For each interval the current crack velocity was calculated using equation 5. From this crack velocity the crack growth during the interval was calculated and added to the current crack dimension calculated in the previous interval. In the calculations the appropriate values for K_{IC} (0.75 $MNm^{-3/2}$) and maximum crack velocity (1500 $m\ s^{-1}$) have been used.

(vi) From the maximum flaw size after impact the post-impact strength of this specimen was calculated. By comparing the pre and post-impact strength of the specimen,the occurence of impact damage could be determined.

(vii) The above procedure was repeated for a 100 specimens under identical impact conditions. For each impact velocity the average fracture stress and the probability that the fracture stress is reduced by the impact were calculated.

(viii)Finally the initial stress pulse amplitude, i.e. the impact velocity (equation 1), was stepwise increased and the whole procedure was repeated for each pulse amplitude.

The results of the calculations have been plotted in the form of a residual strength curve in Figure 4. A very good qualitative agreement with the residual strength curve for single impact is obtained. In particular the variation in the amount of scatter in the fracture stress as a function of the impact velocity is well-reproduced in the analysis. From the analysis a failure probability curve can be obtained which is also shown in Figure 4 (broken line). Once again a good qualitative agreement with the measured probability curve is obtained. The model has also been used to calculate the effect of multiple impacts on the resulting damage and the same conclusions as from the experimental results can be made, namely an almost constant threshold velocity, a reduction of the width of the transition region and a continuous increase in the post-impact flaw size at high impact velocities.

The model can also be used to illustrate the effect of abrasion on the residual strength curve. For this purpose a new set of specimens with twice the density of flaws was generated. Furthermore, the size of the most frequent defect was increased to 25 μm with 99% of the defects smaller than 100 μm. The impact parameters and material properties were not changed. The residual strength curves for the 'as received' (open circles) and the 'abraded' specimens (closed circles) are plotted in Figure 5. Due to the abrasion not only the initial strength of the specimens is reduced but also the threshold velocity and the post impact strength at high impact velocities. The failure probability curve (not shown) shows a much smaller transition region for the 'abraded' specimens. The above predictions are in very good agreement with experimental data for jet impact studies (23). Furthermore, Wiederhorn and Lawn (24) noted similar effects for solid particle impacts on abraded and unabraded glass specimens.

Finally, in Figure 6 the beneficial effect of increased toughness of the specimens is illustrated. The solid line indicates the residual strength curve for a material with $K_{IC} = 1.5\ MNm^{-3/2}$ (i.e.twice that of the reference material). The other impact and material parameters are as for the reference conditions. It should be mentioned that such an increase in impact resistance can also be obtained by polishing the specimens, i.e. producing smaller flaws with a lower density. However, in practice polishing is not a feasible technique for improving the rain erosion resistance because of the problems associated with maintaining the surface finish.

SECTION III

THE EFFECT OF THIN HARD COATINGS ON THE HERTZIAN STRESS FIELD

1. INTRODUCTION

The elastic contact between brittle solids and spherical indenting or impacting particles may lead to the formation of ring and Hertzian cone cracks. These cracks, which are due to radial tensile stresses in a shallow surface layer around the contact area, cause surface degradation and can lead to significant losses in strength and transparency. This form of contact damage has restricted the use of brittle materials in many high performance/reliability applications. However, since ceramics and glasses possess a wide range of useful properties which are not (or not easily) obtainable from more ductile materials, the integration of brittle components in engineering structures is now frequently desirable if not essential. One way of reducing the damage due to static or dynamic contact is by protecting the surface with a coating. The application of compliant protective coatings is well-established (e.g. plastic-coated bottles and neoprene-coated aircraft radomes)and has been examined in detail Pitts(25); Dhaliwahl and Rau(26); Conway, Lee and Bayer (27); Conway, Engel and Lee (28); Chen and Engel (29); Matthewson (30,31). Of particular interest is recent theoretical work by Matthewson (30,31) in which the indentation stress field is calculated for a compliant coating bonded to a rigid substrate. It is shown that the presence of a coating of appropriate thickness can significantly reduce the maximum radial tensile stress in the substrate and that incompressible materials are most effective. Much of the protection is however lost when coating debonding occurs.

Although metallic and elastomeric coatings have proved their usefulness there are now several practical situations (e.g. infrared transparent aircraft windows) where these traditional coating materials cannot be used because of unsuitable electromagnetic properties. In order to determine the feasibility of protecting brittle substrates by a thin hard coating and to direct the development of new ceramic coating materials, a static finite element model (using the Package for Automatic Finite Element Calculations described by Henshell (32)) is developed in which an undeformable sphere is loaded onto a coated substrate. In the model both the substrate and coating stresses are calculated as a function of the elastic properties of the coating material and the coating thickness and are compared with the analytical solutions for the indentation stress field in a uniform halfspace. The model is described in Section 3.3.

2. THE HERTZIAN STRESS FIELD

The analytical solution of the elastic stress field generated by two spherical bodies in frictionless contact has been determined in general terms by Hertz (33) and has further been developed by Huber (34), Fuchs (35), Huber and Fuchs (36) and Morton and Close (37). Later analyses have considered the effect of friction, Spence (38), Johnson, O'Connor and *Woodward (39), and surface roughness, Greenwood and Trip (40)*, on the stress field generated. In the present work the results for the indentation stress field in composite structures are compared with the analytical solutions for the radial, axial and circumferential stresses as derived by Huber (34).

For a Hertzian contact condition, in which a ball of radius R is pressed onto a flat uniform halfspace by a force F, the radius, a, of the contact zone is given by the well-known equation

$$a^3 = \frac{3}{4} F R \left(\frac{1-\nu_1^2}{E_1} + \frac{1-\nu_2^2}{E_2} \right) \qquad (7)$$

where E_1, ν_1 and E_2, ν_2 are the Young's modulus and the Poisson's ratio of the halfspace and the indenter respectively. The semi-ellipsoidal pressure distribution over the surface of the contact zone is given by

$$\sigma_z = \frac{-3F}{2\pi a^2} \left(\frac{a^2 - r^2}{a^2} \right)^{\frac{1}{2}} \qquad (8)$$

The tangential displacements of the surface due to this pressure distribution are radially inwards and lead to a region of tensile radial stresses around the edge of the contact zone. The radial stress distribution, both within and outside the contact zone, is given by

$$\sigma_r = \frac{3F}{2\pi a^2} \left\{ \frac{1-2\nu}{3} \frac{a^2}{r^2} \left[1 - \left(\frac{z}{\sqrt{u}} \right)^3 \right] + \left(\frac{z}{\sqrt{u}} \right)^3 \frac{a^2 u}{u^2 + a^2 z^2} + \right.$$
$$\left. \frac{z}{\sqrt{u}} \left[\frac{(1-\nu)\, u}{a^2 + u} + (1+\nu) \frac{\sqrt{u}}{a} \operatorname{arctg} \frac{a}{\sqrt{u}} - 2 \right] \right\} \qquad (9)$$

where r is the radial coordinate, and u the positive root of the quadratic equation : $u^2 + a^2 u - r^2 - z^2 = 0$. At the surface and within the contact zone the radial stress distribution is given by

$$\sigma_r = \frac{3F}{2\pi a^2}\left\{\frac{1-2\nu}{3}\,\frac{a^2}{r^2}\cdot\left[1-\left(\frac{a^2-r^2}{a^2}\right)^{3/2}\right]-\left(\frac{a^2-r^2}{a^2}\right)^{1/2}\right\} \tag{10}$$

The radial stress is compressive within the contact zone but is tensile within a shallow surface layer outside the contact zone. In the case of elastic ball indentations on brittle materials, the tensile radial stress outside the contact zone is the most important of the stresses since it can lead to the propagation of surface flaws which cause strength reductions, material removal and surface degradation.

The spacial dependence of the circumferential and axial stresses are given by

$$\sigma_t = \frac{-3F}{2\pi a^2}\left\{\frac{1-2\nu}{3}\,\frac{a^2}{r^2}\left[1-\left(\frac{z}{\sqrt{u}}\right)^3\right]+\frac{z}{\sqrt{u}}\left[2\nu+\frac{(1-\nu)\,u}{a^2+u}-(1+\nu)\,\frac{\sqrt{u}}{a}\,\mathrm{arctg}\,\frac{a}{\sqrt{u}}\right]\right\} \tag{11}$$

and

$$\sigma_z = \frac{-3F}{2\pi a^2}\left(\frac{z}{\sqrt{u}}\right)^3\,\frac{a^2u}{u^2+a^2z^2} \tag{12}$$

where the parameters have the same meaning as in the previous equations. Note that equation 11 is the corrected form of the original Huber equation (41).

3.3 FINITE ELEMENT MODEL FOR SPHERICAL INDENTATIONS ON COATED SURFACES

In this analysis for the static indentation of a coated substrate by an undeformable spherical indenter the effect of the thickness and the elastic properties of the coating are investigated. Throughout the analysis the properties of the substrate are held constant and equal to the properties of glass as given in the PAFEC materials module namely : Young's modulus 61 GPa and Poisson's ratio 0.25. The effect of the coating thickness has been investigated for thicknesses up to 20% of the contact radius, i.e. only thin coatings have been modelled. The Young's modulus of the coating material has been varied between 1 and 10 times that of the substrate material. This range covers nearly all possible hard coating materials (e.g. the Young's modulus of diamond is about 15 times as high as that of the chosen substrate). The Poisson's ratio of the coating has been varied between 0.20 and 0.30. Once again, this range covers the majority of the potential hard coating materials.

The finite element distribution used is shown in Figure 7a. The elements are divided into two groups : one with the (fixed) substrate properties and one with the (variable) coating properties. The elements with the coating properties are shaded in Figure 7b. The thickness, d, of the coating is very small compared with the dimensions of the total structure (less than 2%), so that boundary effects do not interfere with the stress field calculated. It has been verified that in the case of a uniform halfspace (i.e. the coating elements have the same elastic properties as the substrate) the finite element results for the radial, axial and circumferential stress agree with the appropriate analytical solutions. For the chosen element distribution, the difference between the two solutions is always less than 0.5%.

In the analysis only vertical displacements, w, are prescribed to the nodes within the chosen contact zone according to

$$w = \frac{a^2}{R} - \frac{r^2}{2R} \tag{13}$$

In order to model the case of elastic contact accurately, the ratio of the contact radius to the indenter radius is chosen as 1 to 100. Because of the discontinuity in the radial and circumferential stress across the interface the reported stresses at the interface are those calculated for the interface elements with substrate properties. Such an approach gives a true indication of the effect of the various coating parameters on the substrate stress field.

In the following sections the calculated stresses are normalised to appropriate reference stresses. The normalisation was made such that positive values indicate tensile stresses and negative values compressive stresses.

3.4 RESULTS FOR AN EXAMPLE PROGRAM

Before considering the main results, the results of a particular

PAFEC program are shown and discussed. In this example program $E_c = 610$ GPa, $\nu_c = 0.20$, $E_s = 61$ GPa, $\nu_s = 0.25$ and the ratio of the coating thickness to the contact radius = 0.05. The subscripts c and s refer to the coating and substrate material respectively.

The calculated axial stress distribution at the interface is shown in Figure 8. The axial stress is normalised to the maximum axial stress P_o calculated analytically for an indentation of the same contact radius on a uniform halfspace with the substrates properties. The finite element results are indicated in this figure by the closed circles. The dashed line gives the analytical solution for the radial stresses in a halfspace with substrate properties at the depth of the interface. The figure shows that for the same contact radius the axial stresses are larger due to the presence of the stiff coating, as would be expected intuitively. The maximum axial stress is about 10% higher than for Hertzian contact on a uniform halfspace. The spatial distribution of the axial stress in the contact zone is however not changed significantly by the coating. This is illustrated by the good fit between the finite element results and the solid line, which is given by

$$\sigma_z' = P^* \left(\frac{a^2 - r^2}{a^2} \right)^{\frac{1}{2}} \qquad (14)$$

where P^* is the maximum axial stress on the coating surface as calculated by the finite element program. The equation above is identical to the equation for the axial stress (equation 8) derived by Huber (34), apart from the scaling factor P^*.

The circumferential stress at the interface is shown in Figure 9. The same normalisation procedure as for the axial stress field is used. The finite element results are indicated by closed circles. The dashed line shows the Hertzian solution for the hoop stress at the depth of the interface. The solid line is identical to the Hertzian equation for the circumferential stress (equation 11), apart from the scaling factor P^*. This figure shows that the coating reduces the circumferential stresses considerably both within and outside the contact zone. The reduction is due to the restricted displacements of the substrate surface because of the higher stiffness of the rigidly adhering coating.

The radial stress at the interface is shown in Figure 10. The finite element results are again indicated by closed circles. The dashed line is the analytical solution for the radial stress in a uniform halfspace at the depth of the interface. The solid line is a similar modification of the original Huber solution as has been made for the axial and circumferential stresses. The figure shows clearly that the maximum radial stress in the substrate is considerably reduced. This indicates that hard coatings can be used to protect the substrate against damage due to localised loading. The reduction of the radial stresses can be explained in the same way as the reduction in the circumferential stresses, namely, by a reduction of the radial displacements at the interface. This reduction in radial displacements is shown in Figure 11, which shows the radial displacements (normalised to the maximum penetration of the indenter) at the interface for the composite structure and the radial displacements at the depth of the interface for a uniform halfspace (solid line).

Figure 12 shows the interfacial shear stress in a radial direction both for the composite structure and for a 'substrate halfspace' (solid line). For the present coating parameters, the maximum shear stress is more than doubled. This is important since interfacial shear stresses of significant magnitude can lead to the coating debonding, in which case the protection provided by the coating is greatly reduced.

Examination of the stresses at the coating surface has shown that the axial stress or normal pressure at the coating surface is nearly identical to that at the interface as can be expected for any thin coating. The maximum pressure at the centre of the contact is 10% higher than for an uncoated substrate.

The effect of the properties of the coating material on the stresses in the plane of the coating, e.g. the radial and the circumferential stress, is however, very large. This is illustrated in Figure 13 in which the radial stress at the coating surface has been plotted. The figure also includes the radial stress distribution for indentations with the same contact radius on a halfspace with substrate and coating properties respectively. It is shown that within the contact zone the compressive stresses are much higher than for a substrate halfspace but not as high as for a coating halfspace. Outside the contact zone however the radial tensile stresses are more comparable to those for a coating halfspace. The maximum tensile stress for the present coating parameters is nearly equal to the maximum axial stress. For the substrate halfspace the maximum tensile stress is only 16.7% of the central pressure, while for the coating material this ratio is 20%.

3.5 EFFECT OF THE COATING PARAMETERS ON THE AXIAL STRESS

In Figure 14 the maximum pressure, P^*, normalised to the maximum pressure, P_o, for an indentation of the same dimensions on the uncoated substrate, is plotted as a function of the coating parameters, i.e. the coating thickness, its Young's modulus and its Poisson's ratio. Since the pressure distribution on the coating surface is semi-ellipsoidal, this figure is also a plot of the normalised load versus the coating parameters. The figure shows that the maximum axial stress depends primarily on the coating thickness and the Young's modulus of the coating material, but generally the effect is relatively small for these thin coatings. In the figure the maximum pressure for an infinitely thick coating with $\nu_c = 0.25$ (dashed line) is also included. In this case the stress field is identical to that for an indentation on a uniform halfspace. Therefore, for large coating thicknesses the maximum pressure increases linearly with the Young's modulus of the material.

The data plotted in this figure can be easily converted to show the dependence of the contact radius on the applied load for these coated substrates. The results are shown in Figure 15. This figure also shows the analytical solutions for the load dependence of the contact radius for an uncoated substrate and for two coating halfspaces. For the composite structures investigated, the analytical relation between load and contact radius given by equation 7 holds reasonably true, provided the coating thickness is less than 10% of the contact radius.

3.6 EFFECT OF COATING PARAMETERS ON THE RADIAL STRESS IN THE SUBSTRATE

In the analysis presented so far the stress fields in coated and uncoated substrates have been compared for indentations with the same contact radius. However, in such a comparison the total applied load on the indenter varies with the coating parameters. In order to study the effect of the coating parameters for a fixed load, all radial stresses are normalised to the maximum pressure for that particular structure.

The radial stress distribution at the interface is shown in Figure 16 for four different Young's moduli of the coating material. The ratios of the Young's modulus of the coating to that of the substrate are 2,3,5 and 10 respectively. The Poisson's ratios of the coating and substrate material and the coating thickness are held constant at 0.25 and 0.1a respectively. The figure shows that within the contact zone the magnitude of the radial stress decreases with increasing Young's modulus of the coating material. The coating also affects the maximum radial stress at the interface. The reductions of the tensile stresses outside the contact radius are shown in more detail in Figure 17 for the same set of coating conditions. For the stiffest coating investigated, the tensile component of the radial stress field has almost vanished.

The coating not only reduces the magnitude of the maximum radial stress but also affects its position: it is found at increasing radial distance. Since crack propagation in brittle materials depends on both the magnitude of the stress field and the presence of sufficiently large flaws, the above increase in radial distance increases the probability of stressing a major flaw. However, since the radial tensile stress is everywhere smaller than that for an uncoated substrate, these hard coatings do indeed protect the surface.

The effect of the various coating parameters on the maximum radial stress obtained in the substrate is summarized in Figure 18. It should be emphasized that the maximum tensile stress in an uncoated substrate decreases very rapidly with depth below the surface. For a correct interpretation of the effect of the coating, the calculated maximum tensile stress should therefore be compared with the maximum tensile stress in a uniform half-space at a depth identical to the coating thickness (dashed line). The reduction is most sensitive to the Young's modulus and thickness of the coating. For relatively thick coatings the Poisson's ratio of the coating material is also important. The figure shows that the effect of the coating thickness on the reduction of the radial stress is largest for very thin coatings.

3.7 EFFECT OF COATING PARAMETERS ON THE RADIAL STRESS ON THE SURFACE

In contact problems on brittle coating and substrate materials the stresses at the surface of the coating are as important as the stresses in the substrate. Failure of the total structure may be caused by the propagation of flaws located either at the surface or at the interface. The effect of the parameters on the maximum tensile stress at the coating surface, which is also the maximum tensile stress in the total structure, is summarised in Figure 19. These maximum tensile stresses have been determined by extrapolation of the radial stresses outside the contact radius towards the edge of the contact since the program deals with the stress singularity in an imperfect manner. The maximum stress increases initially rapidly with coating thickness for all coatings analysed. Unlike the case of uniform halfspaces, the maximum tensile stress can now be larger than the maximum pressure applied. At larger coating thicknesses the maximum radial stress reaches a maximum value and then decreases again. This behaviour can be explained as follows: for thin coatings the effect of the coating on the stress normal to the plane of the coating, i.e. the axial stress, is rather small. However, the coating has already a large influence on the stresses in the plane of the coating, i.e. on the radial and circumferential stresses. The maximum possible stress at the coating surface is that for an indentation on a coating halfspace with the same contact size. The assumption that the effect of the coating thickness on the maximum pressure can be ignored, leads to the following expression for the maximum radial stress on the coating surface (for a coating material with a Poisson's ratio of 0.25)

$$\sigma_{max} = 0.167\ P_o\ E_c/E_s \tag{15}$$

where P_o is the maximum pressure for a similar indentation on the uncoated substrate. When the coating has a different Poisson's ratio the argument is slightly more complicated, since the effect of the Poisson's ratio on the contact radius has to be taken into account. From the Hertzian solution the following threshold values are derived

$$\sigma_{max} = 0.195\ P_o\ E_c/E_s \tag{16}$$

for a coating material with Poisson's ration 0.20 and

$$\sigma_{max} = 0.137\ P_o\ E_c/E_s \tag{17}$$

for a coating material with Poisson's ratio 0.30. These threshold values are indicated in the figure (dashed lines). A good agreement between the calculated maximum value of the radial stress and the predicted thresholds is obtained for coatings with relatively low Young's moduli. In the case of stiffer coating materials the assumption made is no longer valid and the predicted threshold value should be well above the calculated maximum, as is indeed observed. For very thick coatings the response of the composite structure to the imposed indentation approaches that of a coating halfspace. In that case the ratio between σ_{max} and P^* is given by the appropriate Hertzian solution.

3.8 COATING DEBONDING

In the work presented so far attention has been focussed on the effect of the coating properties on the tensile radial stress component i.e. on the brittle failure mode of the composite structure. It is shown that a stiff coating will reduce the radial displacements at the interface and hence the radial stresses in the substrate. Since the protective influence of the coating is based upon good adhesion across the interface, hardly any protection will be offered by these thin coatings when debonding occurs. The debonding is determined by the shear strength of the interface and the shear stresses due to the applied load. In the case of polymer coatings it has been observed that the shear strength of the coating also depends on the magnitude of the normal component of the load (42). No such information is available for ceramic coatings but the effect will probably be negligible for this type of material. Finally, the critical conditions for coating debonding depend also on the magnitude of the pre-existing stresses at the interface. This is an important problem for hard coatings, in particular for coatings produced by chemical vapour deposition processes where the deposition takes place at elevated temperatures. On cooling down, residual stresses will develop due to differences in the thermal expansion coefficients of the coating and substrate materials. The magnitude of these stresses increases with coating thickness and therefore limits the maximum coating thickness which can be deposited before spontaneous coating debonding occurs.

The interfacial shear stress is plotted in Figure 20 as a function of the coating thickness for constant coating properties ($E_c = 10\ E_s$; $\nu_c = 0.20$). The maximum shear stress is only weakly dependent upon the coating thickness but seems to reach a maximum for a coating thickness of about 10% of the contact radius. For very thin coatings the region of high shear stress is localised around the contact edge. For thicker coatings high shear stresses are generated over a much larger agrea. Qualitatively the same observations are made for coatings with different elastic properties.

Figure 21 shows the calculated interfacial shear stresses for three coating stiffnesses (2,5 and 10 E_s). The other coating parameters, thickness (0.1a) and Poisson's ratio ($\nu = 0.25$), are kept constant. The maximum shear stress increases with the Young's modulus of the coating material. Furthermore, high shear stresses are found over larger areas for higher coating stiffnesses.

Examination of the effect of the Poisson's ratio has shown that the shear stresses are virtually independent of the Poisson's ratio for the limited range investigated; this applies in particular to the very rigid coatings. The same result has been obtained by Matthewson (30) for thin compliant coatings with Poisson's ratios in the range 0.2 to 0.3. However, his model showed that the inferfacial shear stress increases rapidly for Poisson's ratios approaching 0.5.

3.9 CONCLUSIONS

It has been shown that thin hard coatings reduce the maximum tensile stress in the substrate but also increase the maximum stress in the composite structure compared to the values for an uncoated halfspace. Thin hard coatings can therefore be used to protect brittle materials against elastic contact damage. Although the stress reduction is a very important indication about the coating performance, more specific predictions can only be made when information is available on other factors such as the fracture toughness of the coating and substrate material, the interfacial strength, pre-existing stresses and the flaw size distribution.

With regard to the selection of optimum coating materials the present analysis has shown that materials with a high Young's modulus give the largest reduction in the substrate stresses and should therefore be preferred provided that the mechanical properties of the coating material are good enough to withstand the high stresses which develop in the coating. Although the range of Poisson's ratios for hard materials is rather small, materials with a relatively high Poisson's ratio (about 0.3) should be chosen since both the maximum substrate and the maximum coating stress decreases with increasing Poisson's ratio.

When considering the optimum coating thickness it should be noted that the analysis indicates two regions of suitable coating thicknesses, namely very thin ($d/a < 0.05$) or relatively thick coatings ($d/a > 0.4$). For the relatively thick coatings the maximum substrate stresses are virtually independent of the coating thickness while the maximum coating stresses decrease with increasing coating thickness. However, for these thick coatings the problem of spontaneous coating debonding due to residual stresses is a serious one. For the thin coatings a sizeable reduction in the substrate stresses is obtained without too large an increase in the maximum coating stress. Ball indentation experiments on carbon-coated germanium by van der Zwaag and Field (43) have shown that it is indeed possible to obtain a significant increase in the critical load for crack nucleation using thin rigid coatings.

SECTION IV

THE EFFECT OF THIN HARD COATINGS FOR A LOCALLY APPLIED UNIFORM PRESSURE

4.1 INTRODUCTION

In this section we will examine the effect of coating thickness and the elastic properties of the coating material on the surface and interface stresses for the case of a locally applied uniform pressure. The same finite element model as used in the previous section was employed apart from a change in the prescribed loading condition : a uniform pressure over the chosen contact radius instead of a spherical indentation.

We will also compare the static and transient stress field in a uniform halfspace due to such a loading condition to find the limitations of a static model in describing impact phenomena.

4.2 RESULTS FOR AN EXAMPLE PROGRAM

The same coating parameters as used in the example program in section 3.4 were chosen to demonstrate the effect of a hard coating on the stress field due to a local uniform pressure : $E_c = 610$ GPa; $\nu_c = 0.20$; $E_s = 61$ GPa and $\nu_s = 0.25$ and the ratio of the coating thickness to the contact radius = 0.05.

The calculated radial stress distribution at the coating interface is shown in Figure 22. The radial stress is normalised to the pressure prescribed to the surface nodes within the contact zone area. The finite element results are indicated with closed circles. The dashed line in the figure indicates the radial stress in a uniform halfspace at the depth of the interface. Even for this small coating thickness the coating has a considerable effect on the radial stress field both within and outside the contact area. The same applies to the hoop stress field which is plotted in Figure 23 for both the coated and uncoated condition. The effect of such a thin coating on the magnitude of the axial stresses (not shown)is however negligible for the present loading condition. The shear stress field at the interface is shown in Figure 24. The figure shows that there is a large shear stress which reaches its maximum at the contact radius. The radial stress at the coating surface is plotted in Figure 25. For this small coating thickness the increase in the radial stress at the coating surface is already considerable and is due to the relatively large deflections of the substrate.

In conclusion, the picture which emerges from this example is qualitatively the same as for the example program in the previous section.

4.3 EFFECT OF THE COATING PARAMETERS ON THE RADIAL STRESS

The radial stress distribution at the interface is shown in Figure 26 for three different Young's moduli of the coating material (2,5,10 times that of the substrate). The Poisson's ratio of all coatings is 0.25 and the coating thickness is 0.1 a. The same tendency is observed as for the ball indentation calculations presented in the previous section; namely, a reduction of the radial stress outside the contact radius with increasing coating stiffness and an increase in the radial distance at which the maximum radial stress is reached.

The effect of all the coating parameters on the maximum radial stress at the interface between coating and substrate is summarised in Figure 27.

The effect of the elastic properties of the coating and its thickness on the maximum tensile stress in the coating surface is plotted in Figure 28. As is already shown in Figure 25 this maximum occurs at or near the edge of the loaded area. Also for the present loading conditions the maximum tensile stress at the surface is considerably higher than that for the uncoated substrate. When comparing the thickness dependence of the maximum surface stress with that for a spherical indentation (Figure 19) it will be clear that a uniform pressure over the contact area causes a larger increase in the surface stresses and that the coating thickness at which the highest tensile stresses occur is smaller. These differences are due to the differences in the magnitude of the pressure near the edge of the contact zone. The influence of the elastic properties of the coating material on these curves is comparable for the two loading conditions.

4.4 DYNAMIC AND STATIC STRESS FIELD DUE TO A UNIFORM PRESSURE

The solution of the transient stress field in a uniform halfspace due to a uniform pressure over an expanding contact area has been determined by Blowers (44). His model is a simplification of the pressure distribution in a solid target due to an impacting drop. Recent theoretical (4,45,46) and experimental work (47,48) has shown that the pressure which develops during the initial stages of the impact is not very uniform but rises sharply towards the edge of the contact area. However, Adler (49) concludes from the good agreement between the Blowers result and a more complex finite difference model in which both the liquid drop and the target are considered (46), that the contribution of the edge pressure to the transient radial stress field is very small.

The normalised radial stress field calculated according to Blowers model depends on both the material properties and the impact velocity;

unlike the static case where the normalised stress field depends on the material properties only. Examples of the transient radial stress field (normalised to the impact pressure P) are shown in Figure 29 for a 200 m s^{-1} and a 600 m s^{-1} drop impact on zinc sulphide respectively. It will be clear from these figures that the spatial distribution of the transient radial stress is very different from that for the static case where the surface stress outside the contact area is given by (50)

$$\sigma_r = \frac{1 - 2\nu}{2} P_o \frac{a^2}{r^2} \qquad (18)$$

Furthermore, the figures show that the ratio of the maximum tensile stress and the applied pressure is impact velocity dependent; for the static case the ratio is 0.25, for an impact velocity of 200 m s^{-1}, 0.9 and for a 600 m s^{-1} impact 1.6. This increase is due to the fact that with increasing impact velocity the contact area expands faster. Since the stress wave velocity in the material remains constant, the pulse energy becomes more localised, i.e. the resulting stresses are increased.

4.5 DISCUSSION

It has been shown that for the present loading condition, i.e. a locally applied uniform pressure, hard coatings can reduce the maximum tensile stress in the substrate and that the reduction depends primarily on the coating thickness and the Young's modulus of the coating material.

The effect of the coating parameters on the maximum tensile stress both in the coating and the substrate is about the same as for the spherical indentation; in particular the ranking of the optimum elastic properties of the coating material is identical.

The comparison between the static and dynamic stress field in a uniform halfspace due to a uniform pressure has shown that there are considerable differences both in the distribution and the magnitude of the radial stresses. The differences between the static and dynamic stress fields will be even larger for layered structures since in the second case the final stress field will be the sum of the surface or Rayleigh wave, the interface or Stoneley wave and the various incident and reflected bulk stress waves. Furthermore, the type of stress wave will depend on the ratio of the wavelength and the coating thickness. Although equations for various elastic waves in layered structures have been developed (see for a general introduction Ewing et al (51)) the complete solution of the simultaneous effect of all the stress waves on the final stress field at the interface and in the coating will require considerable effort; in particular for loading conditions as complex as during liquid drop impact.

The relevance of the present work with respect to protection against rain erosion damage should therefore be seen in the light of protecting the substrate from contact damage during handling and exposure to (quasi-static) dusty atomospheres, since a reduction of the initial flaw size will cause a reduction in the high velocity rain impact damage in brittle materials, as demonstrated in the model presented in Section 2. However, recent experiments on carbon-coated germanium (43) have shown that hard coatings can provide protection against contact damage for static (ball indentations) as well as dynamic (liquid jet impact) loading conditions.

REFERENCES

1. Field, J.E., Matthewson, M.J. and van der Zwaag, S., Annual Report, 1979, AFOSR-78-00125.
2. Field, J.E., van der Zwaag, S. and Hagan, J.T., Annual Report, May, 1981, AFWAL-TR-81-4026.
3. Field, J.E., Lesser, M.B. and Davies, P.N.H., 1979, Proc. 5th Int. Conf. on Erosion by Liquid and Solid Impact (ELSI V) Cavendish, Cambridge, UK paper 2.
4. Lesser, M.B., 1981, Proc. Roy. Soc. A377, 289.
5. Gorham, D.A. and Rickerby, D.G., 1975, J. Phys. E. Sci. Instrum., 8 794.
6. Matthewson, M.J. and Field, J.E., 1980, J. Phys. E. Sci. Instrum. 13 355.
7. Rickerby, D.G., 1977, Ph.D. Thesis, University of Cambridge.
8. Bowden, F.P. and Field, J.E., 1964, Proc. Roy. Soc. A282, 331-352.
9. Swain, M.V. and Hagan, J.T., 1980, J. Mat. Sci. 15, 387-404.
10. Sih, G.C., Embly, G.T. and Ravera, R.J., 1972, Int. J. Sol.Struct., 8, 977-993.
11. Freund, L.B., 1972, J. Mech. Phys. Sol., 20, 129-140.
12. Fruend, L.B., 1974, J. Mech. Phys. Sol. 22, 137-146.
13. Broberg, K.B., 1960, Ark. Phys. 18, 159-192.
14. Eshelby, J.D. 1970, Ed. Kanninen, McGraw-Hill, NY.
15. Achenbach, J.D. and Neiusmer, R., 1971, Int. J. Fract. Mech., 7, 77-88.
16. Rose, L.F.R., 1976, Int. J. Fract. Mech. 12, 799-813.
17. Aoki, S., Kishimoto, K., and Sakata, M., 1979, Eng. Fract. Mech. 11 301-314.
18. Kishimoto, K., Aoki, S. and Sakata, M., 1980, Int. J. Fract. Mech. 16 3-13.
19. Kerkoff, F. and Richter, H.,1969, Proc. 2nd Conf. on Fracture, Brighton.
20. Hunt, R.A. and McCartney, L.N., 1979, Int. J. Fract. 15, 365-375.
21. Jayatilaka, A.De S. and Trustrum, 1977, J. Mat. Sci. 12, 1426-1430.
22. Rickerby, D.G., 1980, J. Mat. Sci., 15, 2466-2470.
23. Matthewson, M.J., Cavendish Lab., Private Communication.
24. Wiederhorn,S.W. and Lawn, B.R., 1977, J. Amer. Soc. 60, 451-458.
25. Pitts, E., 1970, J. Phys. D. Appl. Phys. 3 1803.
26. Dahliwahl, R.S. and Rau, J.S., 1970, Int. J. Eng. Sci. 8, 843.

27. Conway, H.D., Lee, H.C. and Bayer, R.G., 1970, J. Appl. Mech. 37 159

28 Conway, H.D., Engel, P.A. and Lee, H.C., 1972, Int. J. Mech. Sci. 14, 523.

29. Chen, W.T. and Engel, P.A., 1972, J. Solids, Struct. 8, 1257.

30. Matthewson, M.J., 1981, J. Mech. Phys. Sol. 29, 89.

31. Matthewson, M.J., 1981b, to appear in J. Phys. D. Appl. Phys.

32. Henshell, R.D. (ed), PAFEC 75: Theory and Results, PAFEC Ltd. Nottingham, UK.

33. Hertz, H., 1881, J. Reine u. Angew Math. 92, 156.

34. Huber, M.T., 1904, Ann. Phys. 14, 153.

35. Fuchs, S., 1913, Phys. Z. 14, 1282.

36. Huber, M.T. and Fuchs, S., 1914, Phys. Z. 15, 298.

37. Morton, W.B. and Close, L.J., 1922, Phil. Mag. 43, 320.

38. Spence, D.A., 1968, Proc. Roy. Soc. A305, 55.

39. Johnson, K.L., O'Connor, J.J. and Woodward, A.C., 1973, Proc. Roy. Soc. A334, 95.

40. Greenwood, J.A. and Trip, J.H., 1967, J. Appl. Mech. 89, 153.

41. Hamilton, G.M. and Goodman, L.E., 1966, J. Appl. Mech. 33, 371.

42. Briscoe,B.J., Scruton, B. and Willis, F.R., 1973, Proc. Roy. Soc. A333, 99.

43. van der Zwaag, S. and Field, J.E., 1981, to be published.

44. Blowers, R.M., 1969, J. Int. Math. Appl. 5, 167.

45. Heymann,F.J., 1967, Proc. 2nd Int. Conf. on Rain Erosion and Allied Phenomena, Meersberg.

46. Rosenblatt, M., Eggum, G.E., De Angelo, L.A. and Kreyenhagen, K.N., 1976, AFML-TR-76-193.

47. Johnson, W. and Vickers, G.W., 1973, J. Mech. Eng. Sci. 15, 302.

48. Rochester, M.C. and Brunton, J.H., 1974, in ASTM-STR 567, page 128.

49. Adler, W.F., 1977, Office of Naval Research publication TR-77-49.

50. Johnson, K.L., 1977, Private Communication, University of Cambridge

51. Ewing, N.M., Jardetzky, W.S. and Press, E., 1957, "Elastic Waves in Layered Media" McGraw Hill, New York.

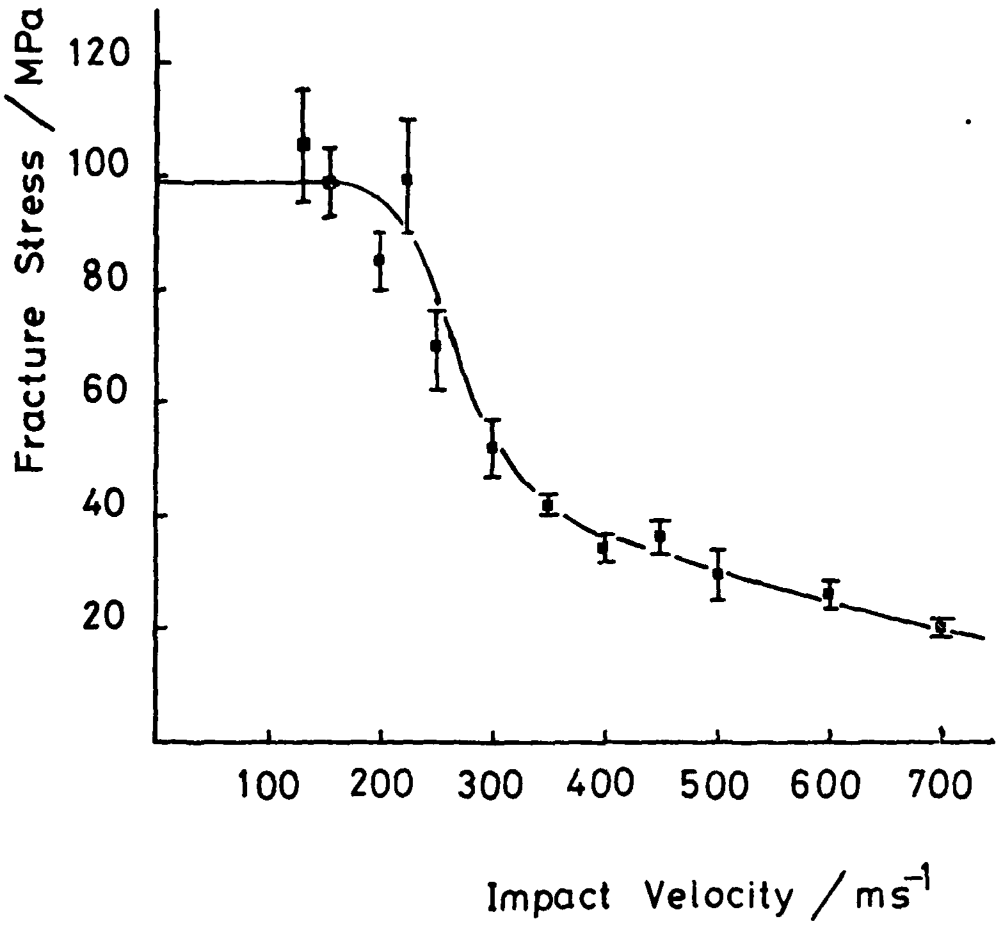

Figure 1. Residual strength curve single impact soda-lime glass jets from 0.8 mm nozzle.

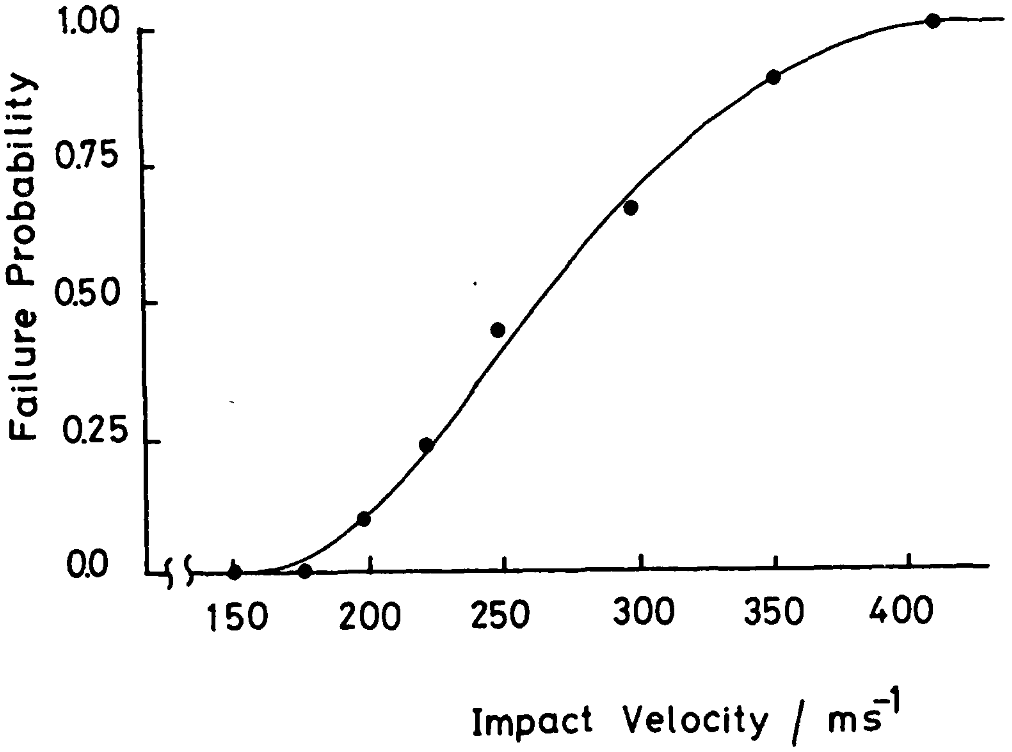

Figure 2. Failure probability curve (same data as in Figure 1)

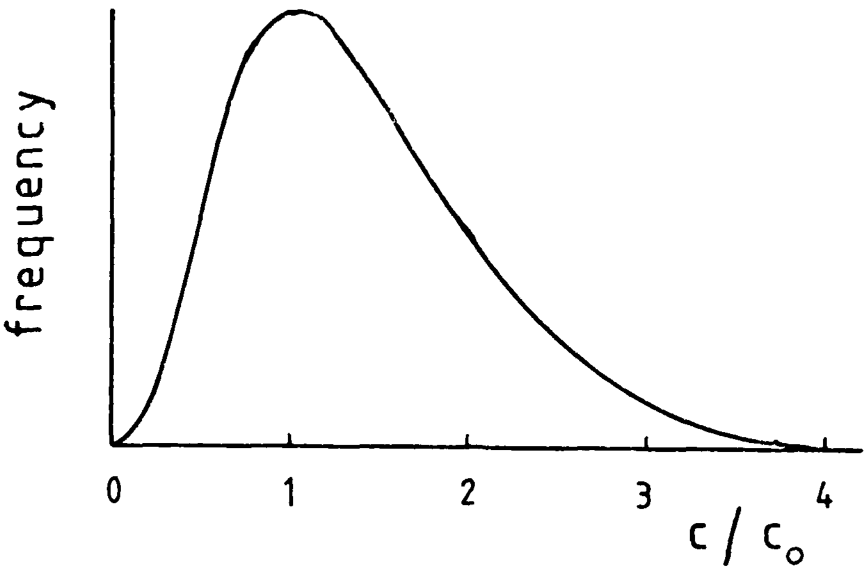

Figure 3. Probability density function for flaw sizes.

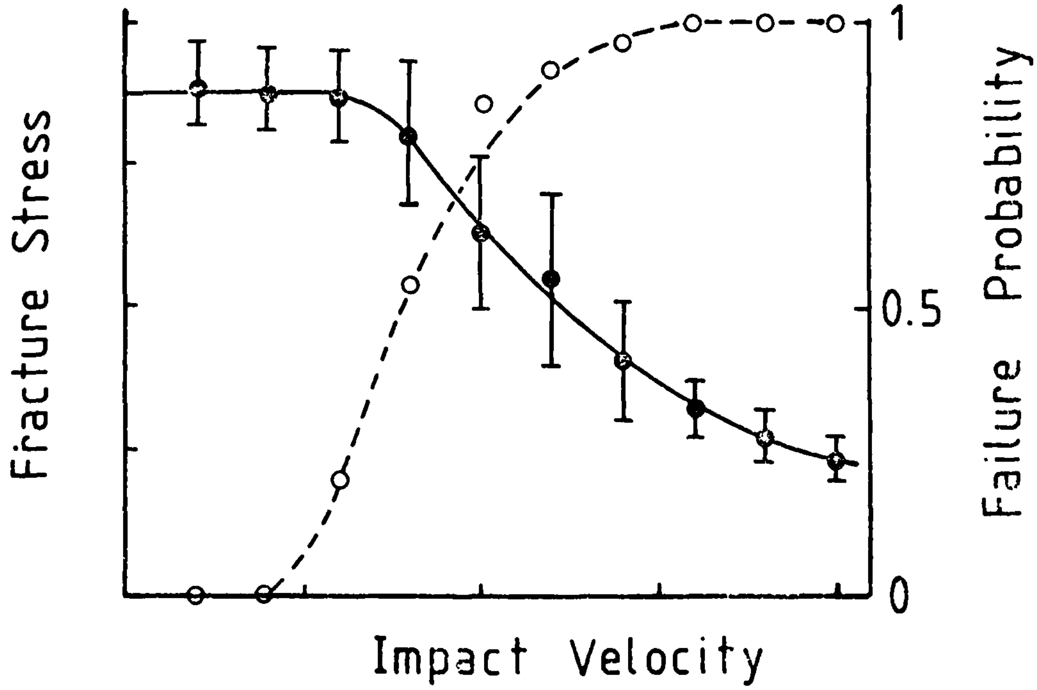

Figure 4. Theoretical residual strength curve (solid line) and failure probability curve (dashed line) for soda-lime glass. (see text).

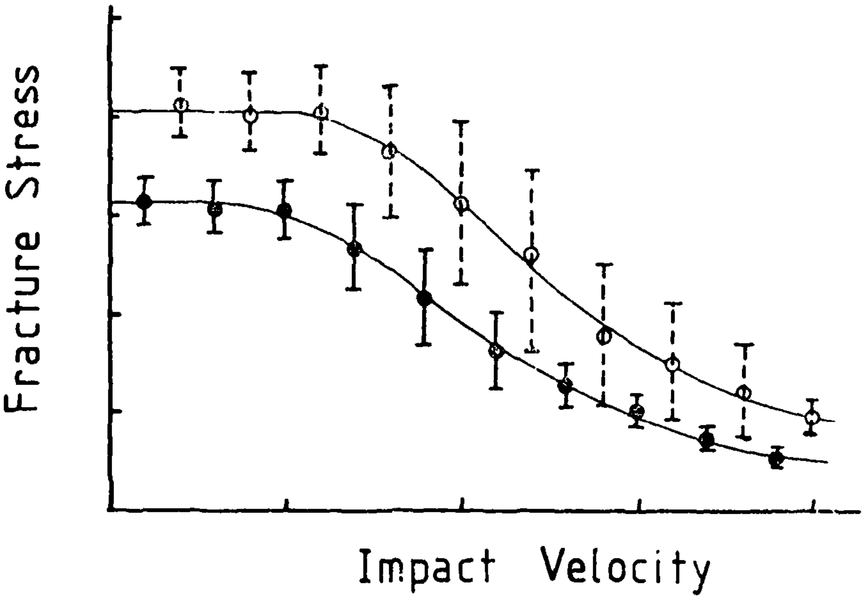

Figure 5. Theoretical residual strength curves for soda-lime glass (see text).

O 'as received' specimens'

● 'abraded' specimens.

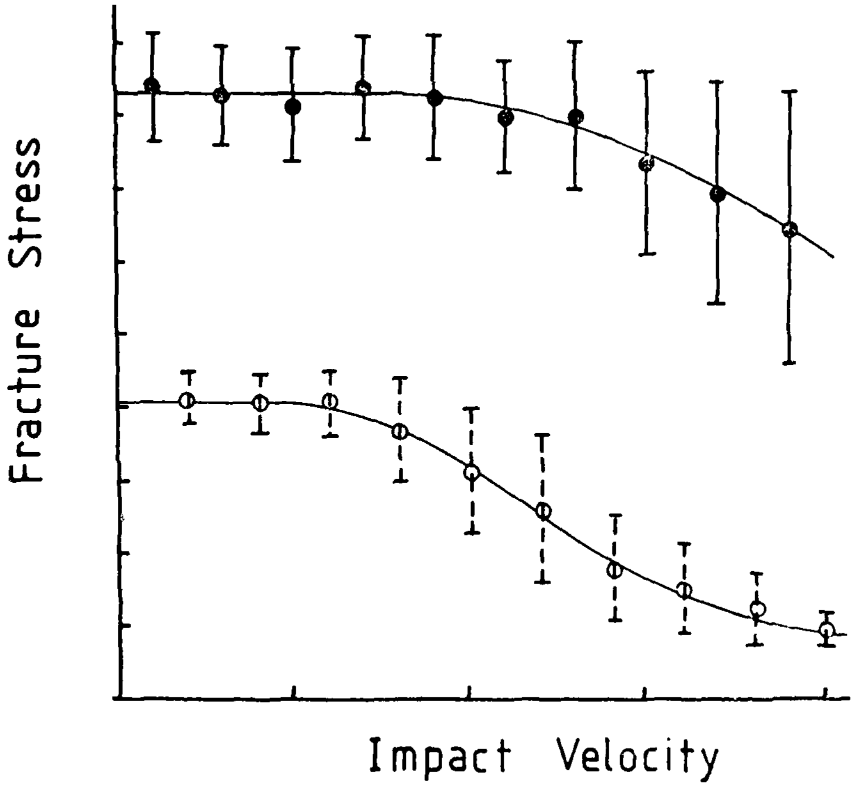

Figure 6. Theoretical residual strength curves for soda-lime glass (O) and 'tough-material' (●).

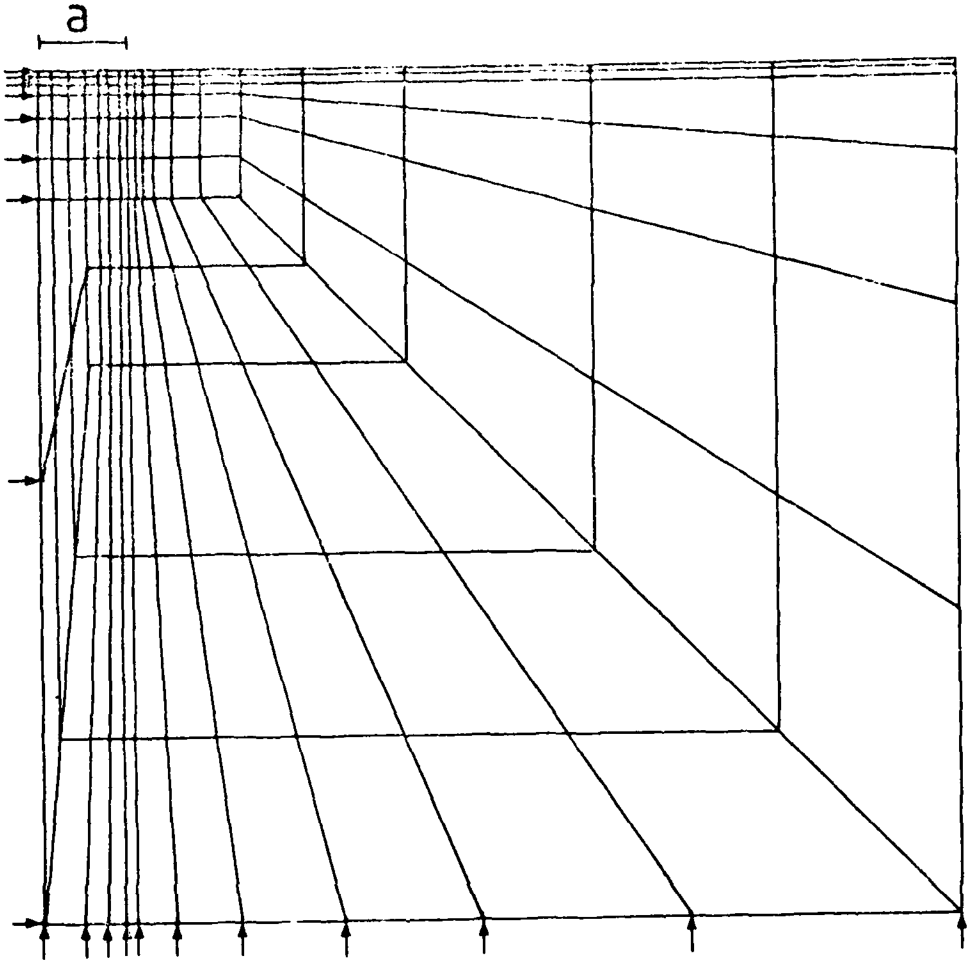

Figure 7a. Finite element distribution for Hertzian indentation on a coated halfspace.

Figure 7b. Detail of 7a. showing the coating elements (shaded) and the substrate elements.

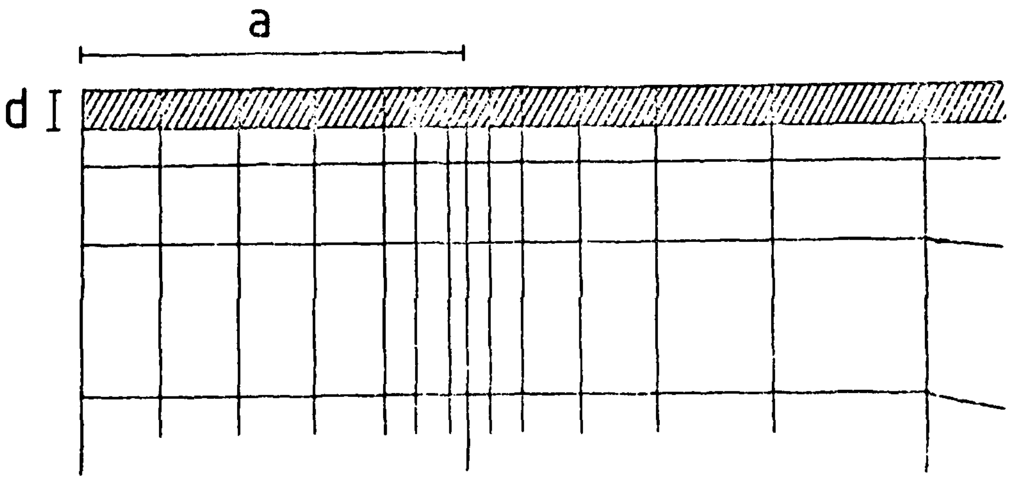

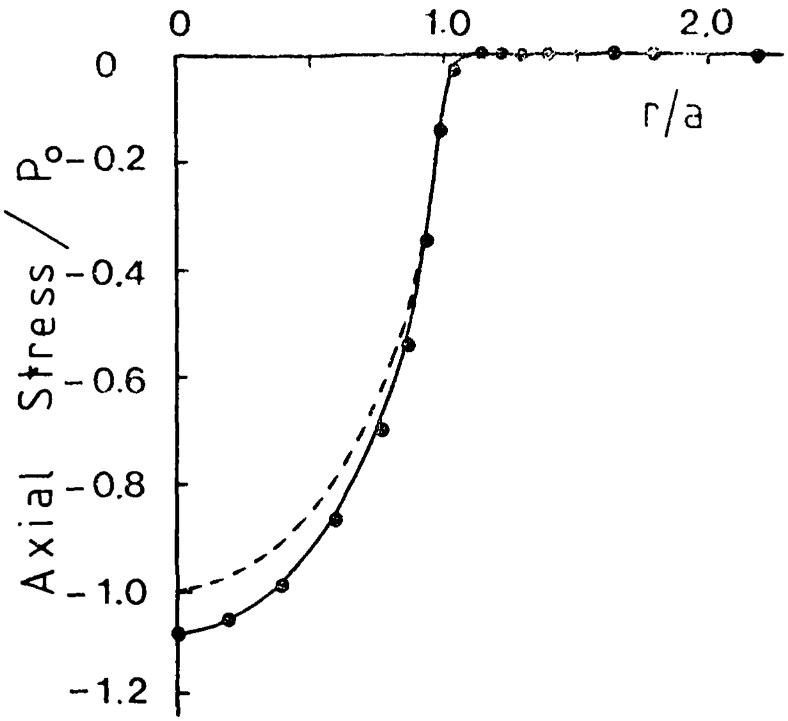

Figure 8. Axial stress at the coating interface (see text).

Figure 9. Circumferential stress at the coating interface (see text).

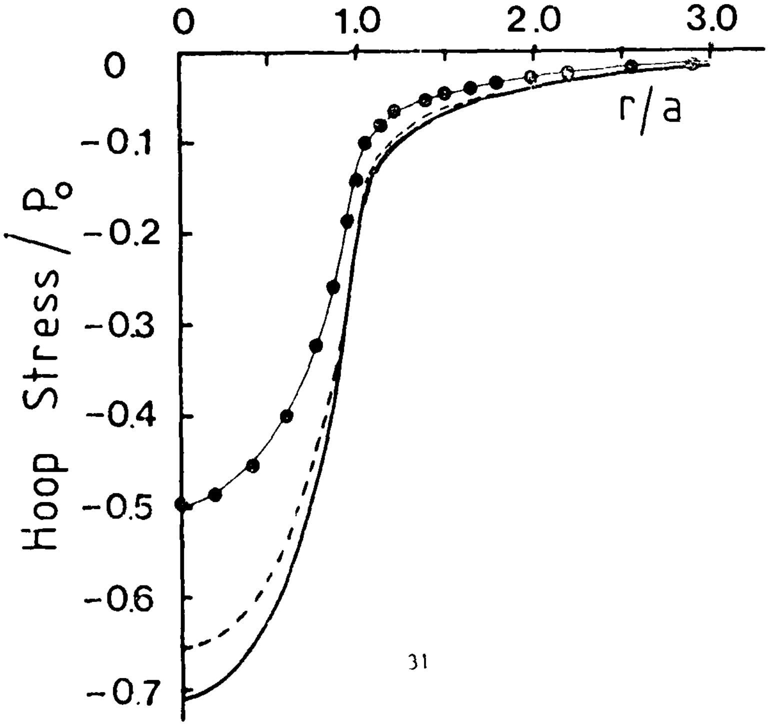

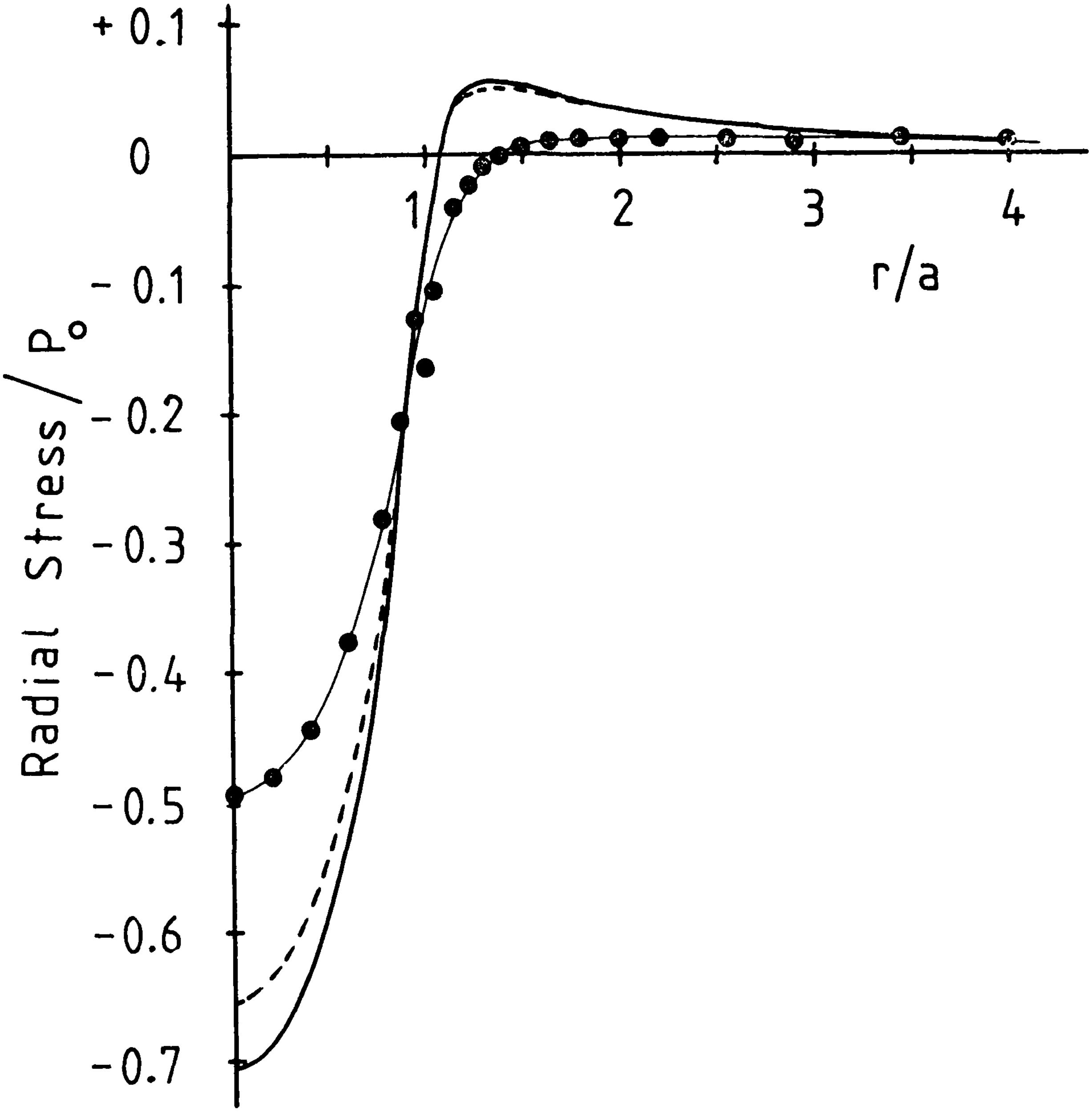

Figure 10. Radial stress at the coating interface (see text).

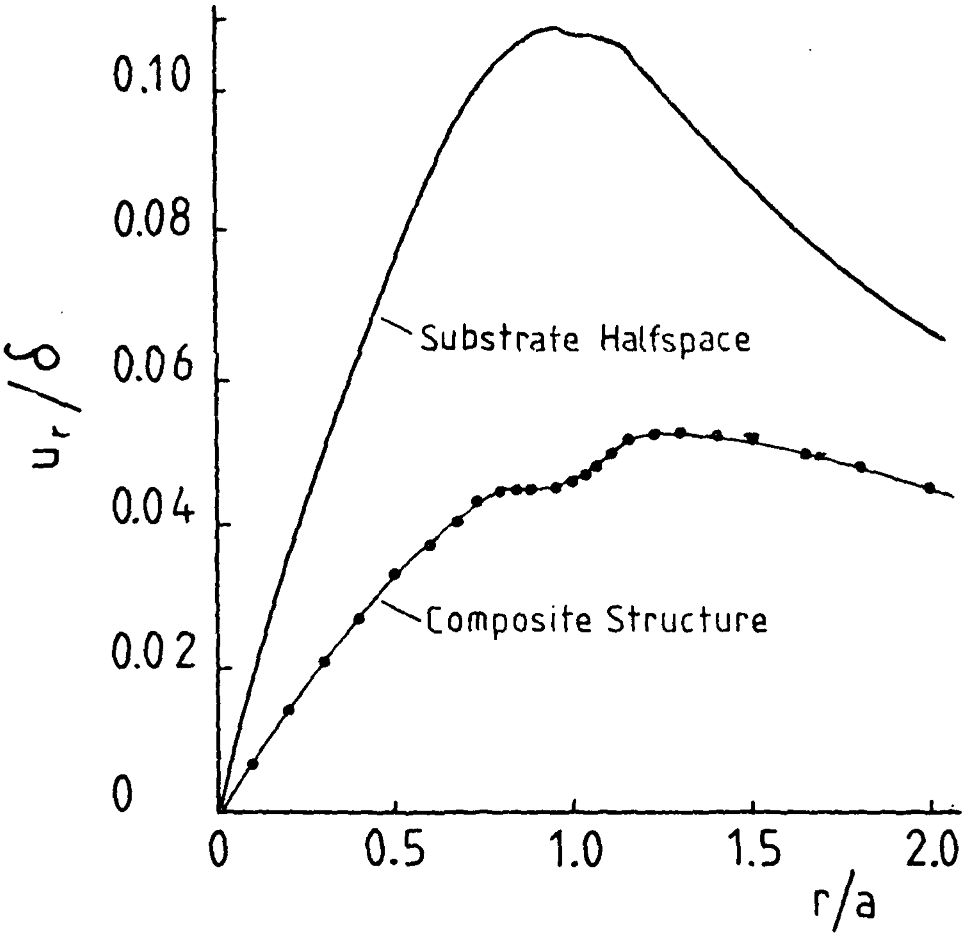

Figure 11. Radial displacements at the interface (see text).

Figure 12. Interfacial shear stress at the interface (see text).

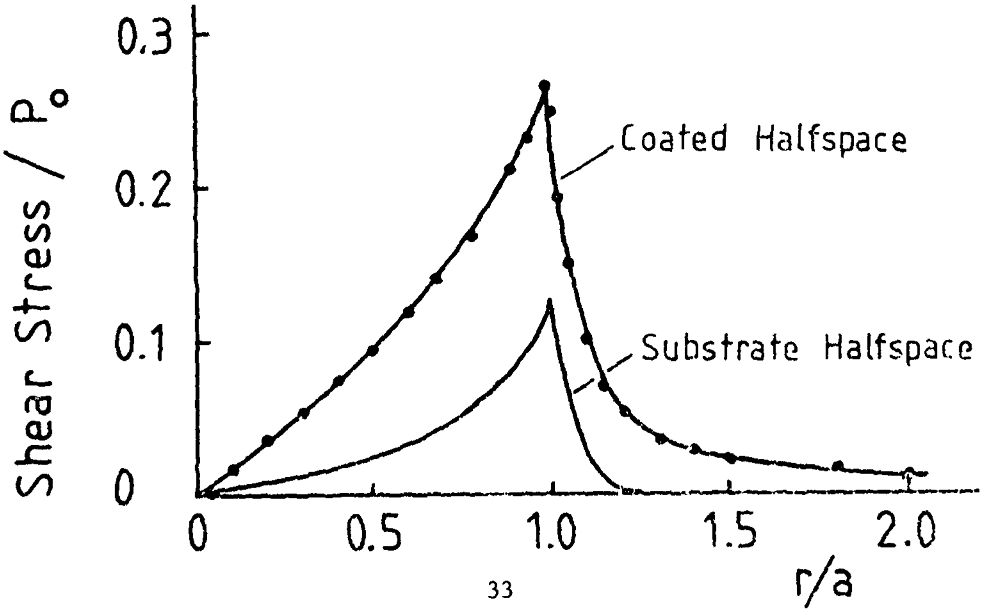

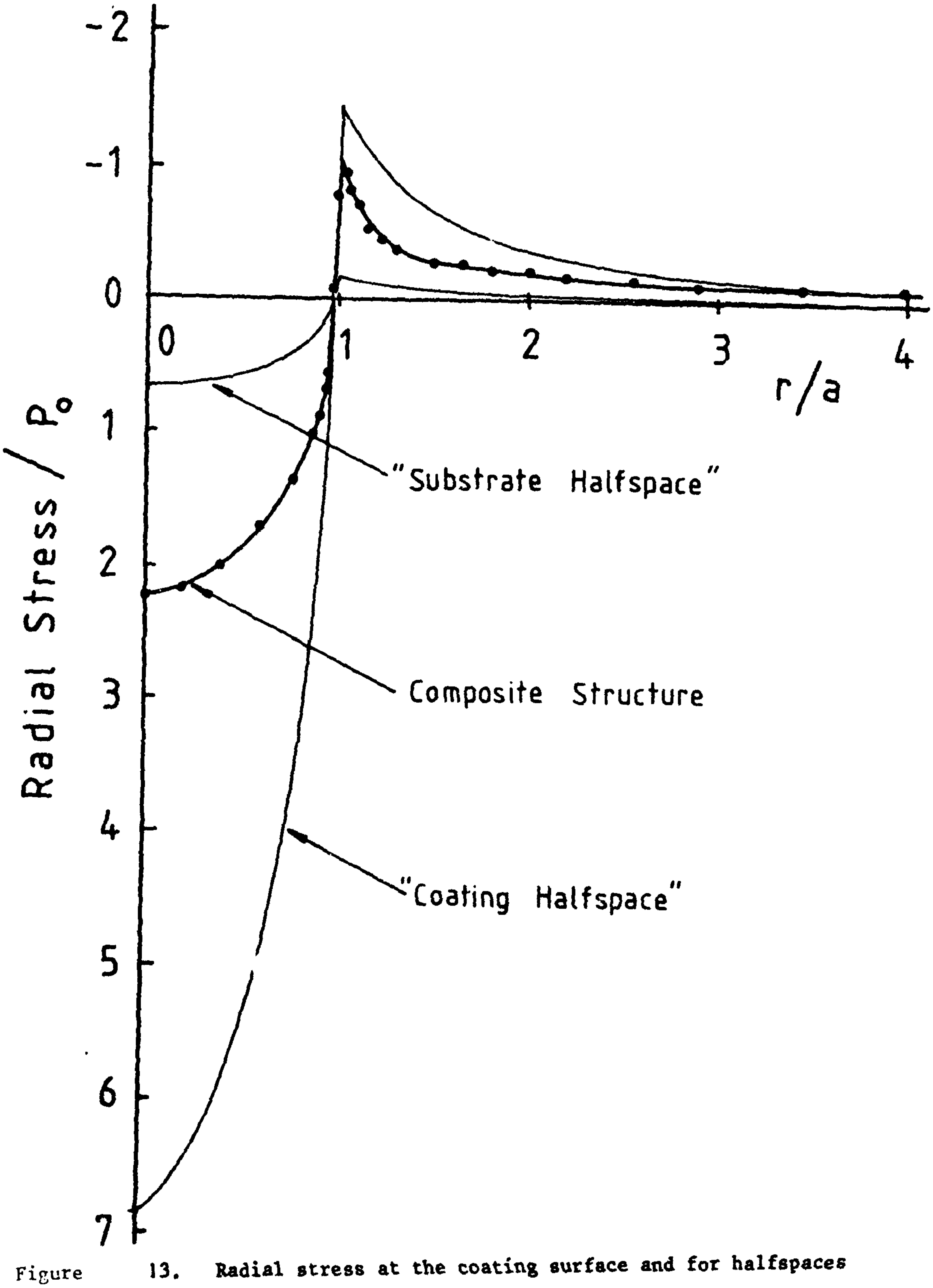

Figure 13. **Radial stress at the coating surface and for halfspaces with coating and substrate properties.**

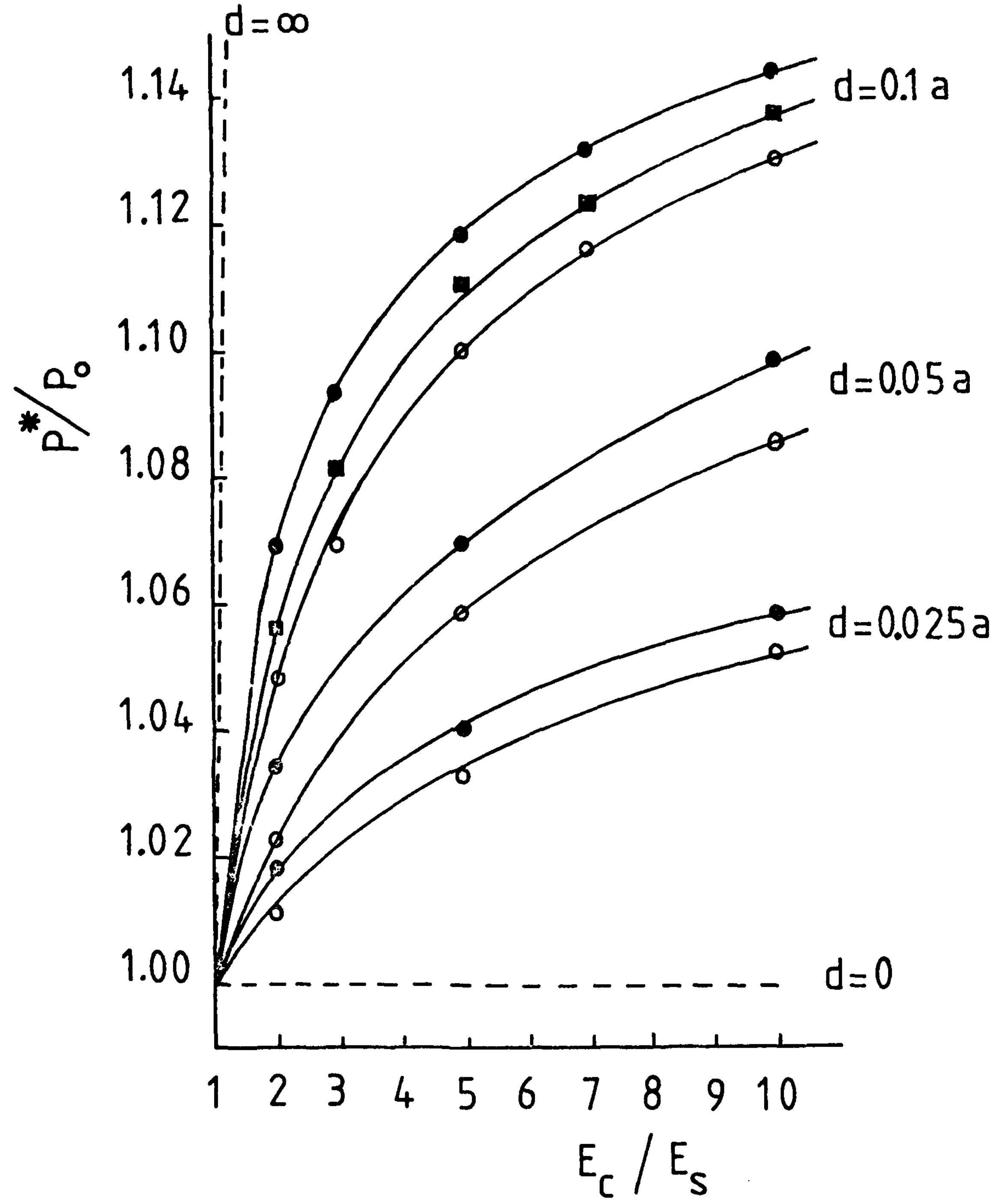

Figure 14. **Variation of the maximum pressure on the coating surface with coating parameters**

● : ν_c = 0.20   ■ : ν_c 0.25   O : ν_c = 0.30

Figure 15. Same data as for Figure 14 but replotted to show the load dependence of the contact radius as a function of the coating parameters ($\nu_c = 0.25$ for all coatings).

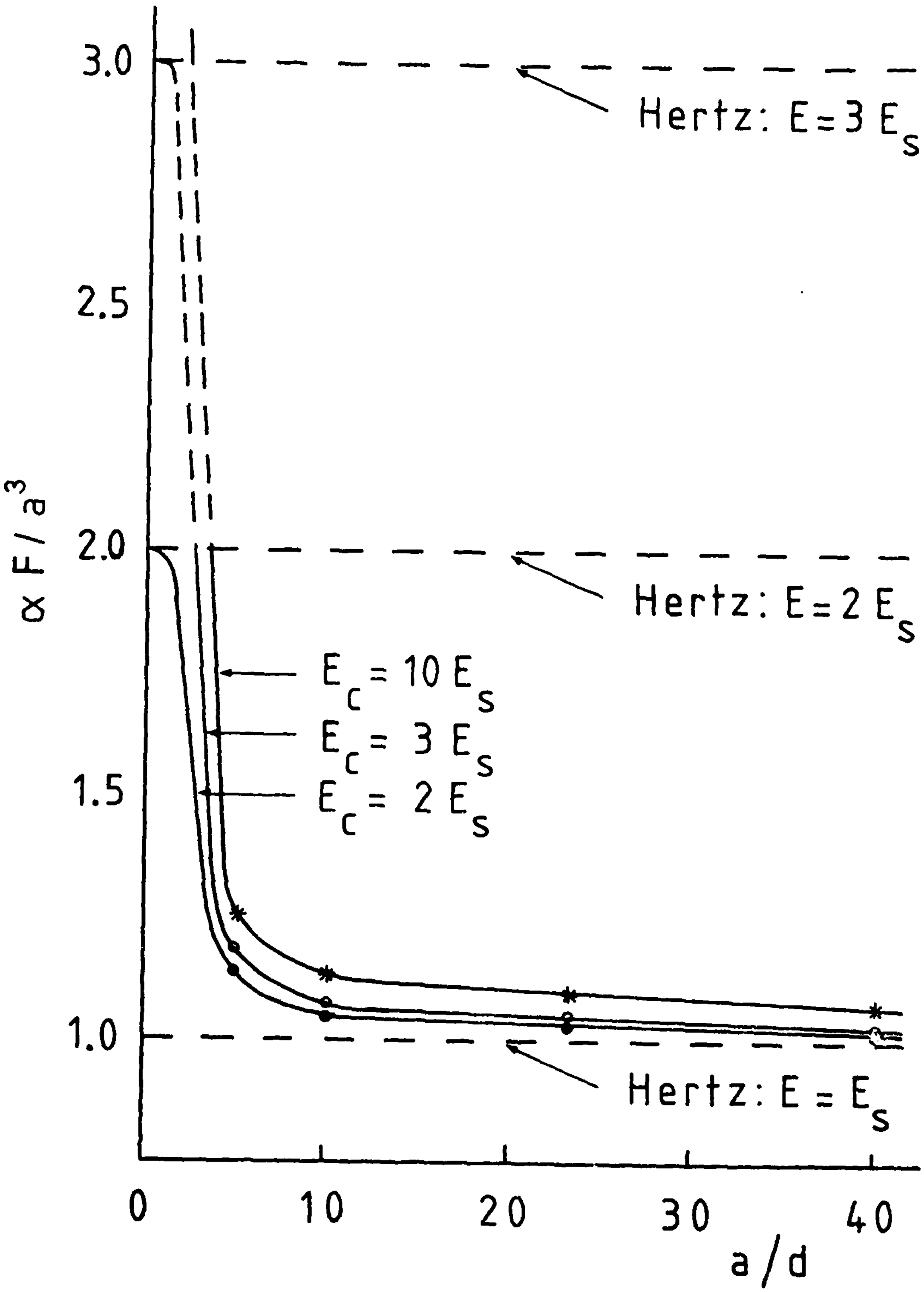

Figure 16. Radial stress at the interface for four different Young's moduli of the coating material. (coating thickness = 0.1a and $\nu_c = 0.25$).

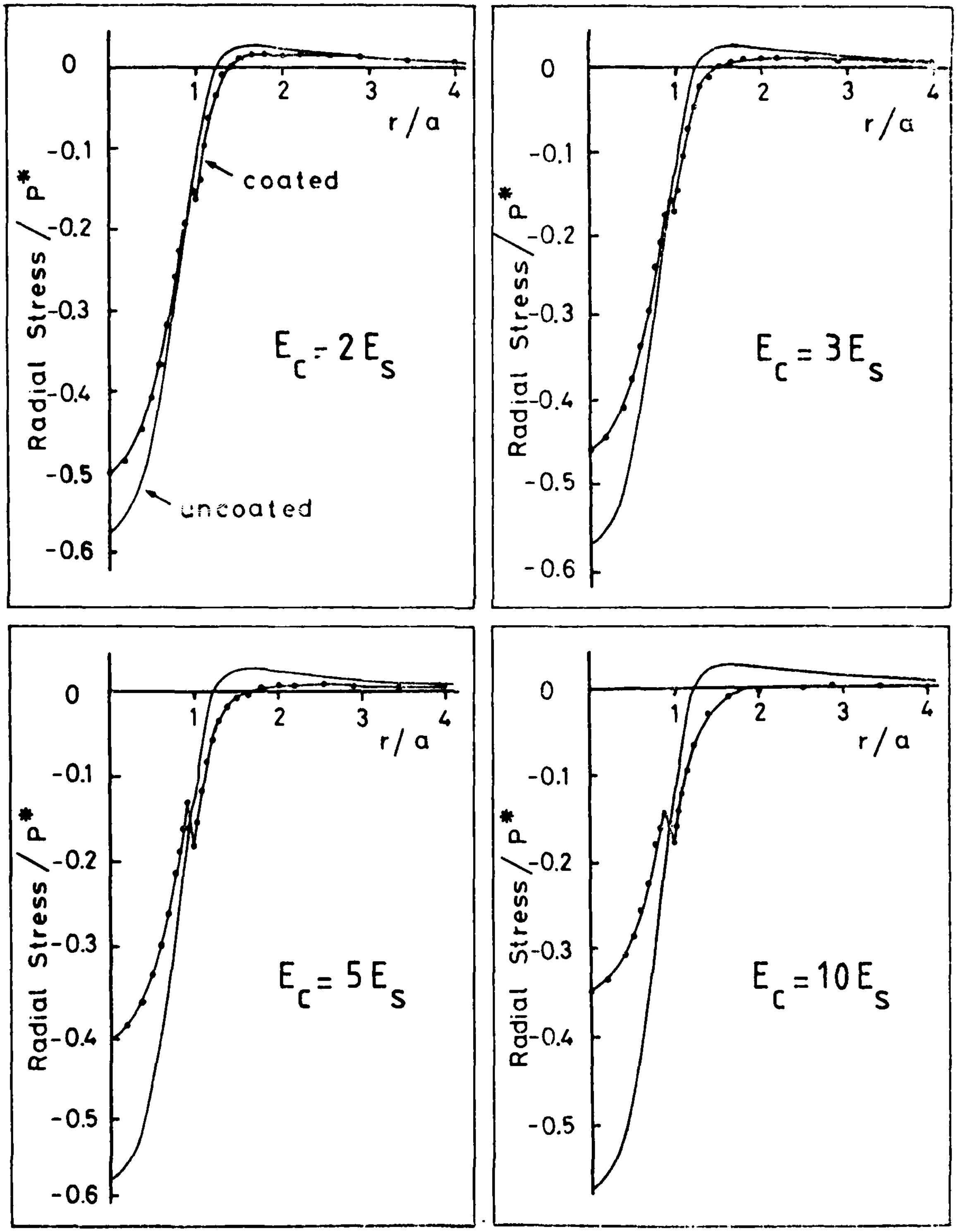

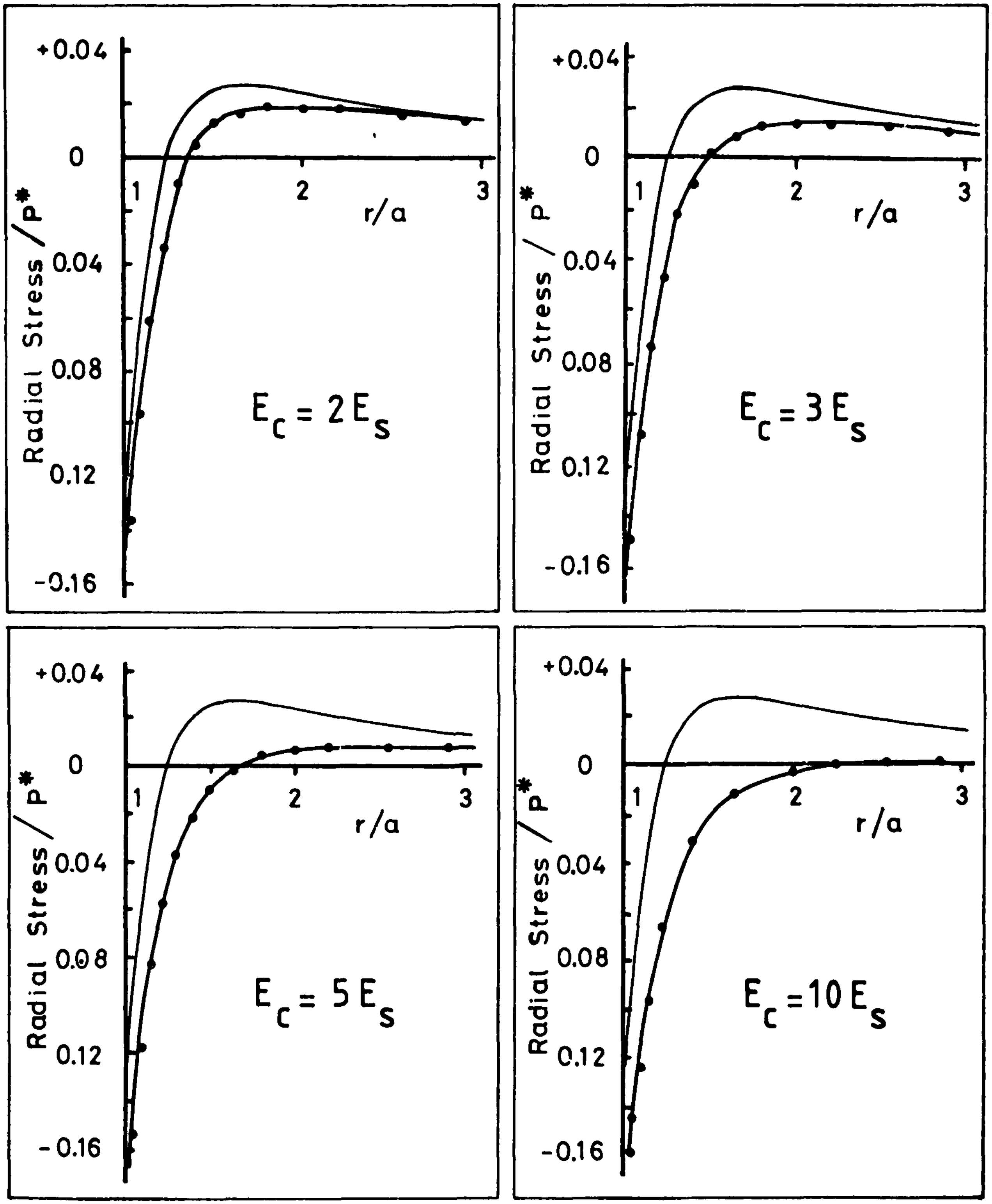

Figure 17. **Radial stress at the interface outside the contact area (same data as for Figure 16).**

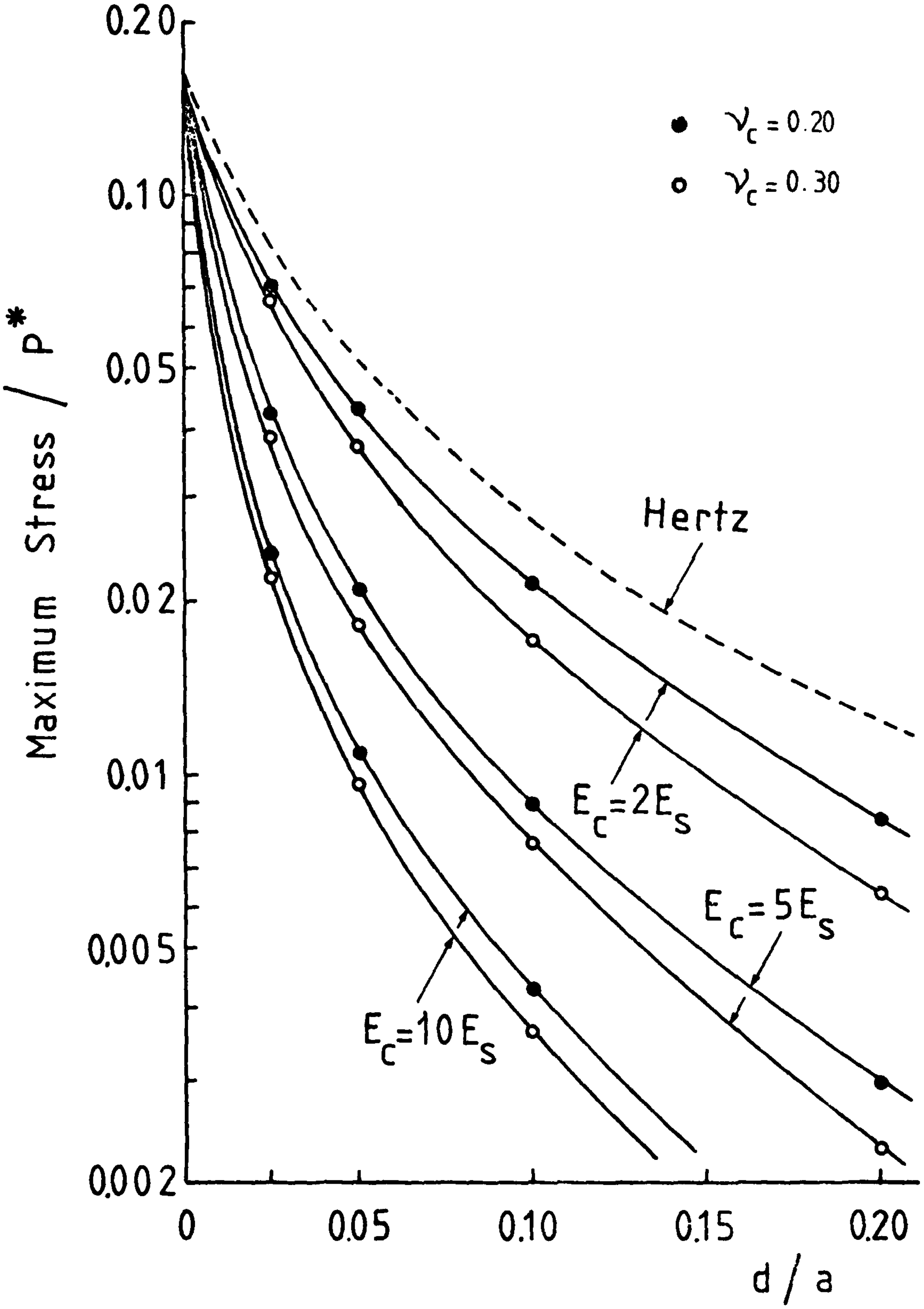

Figure 18. **Variation of the maximum tensile stress at the interface with the coating parameters.**

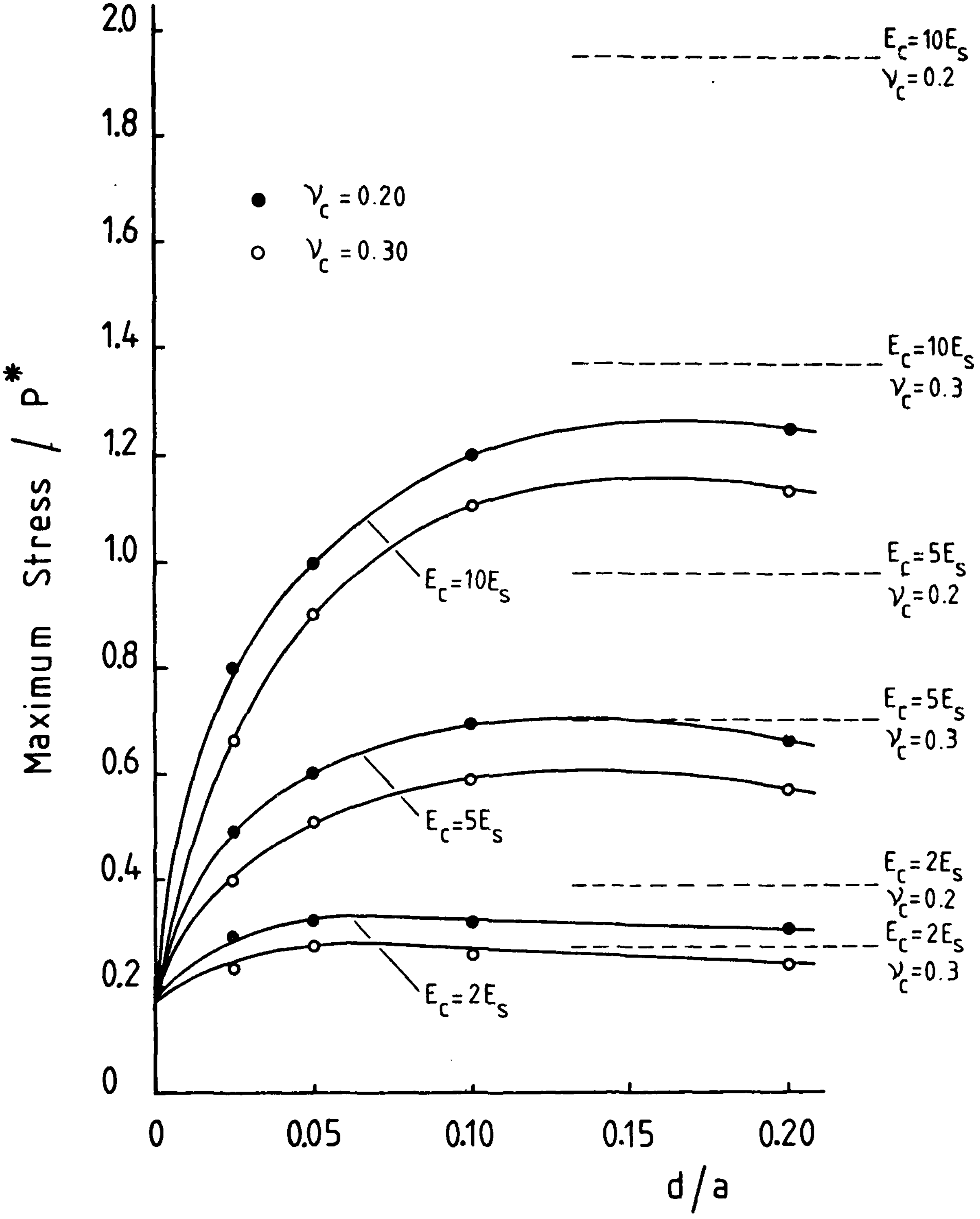

Figure 19. **Variation of the maximum tensile stress at the coating surface with coating parameters.**

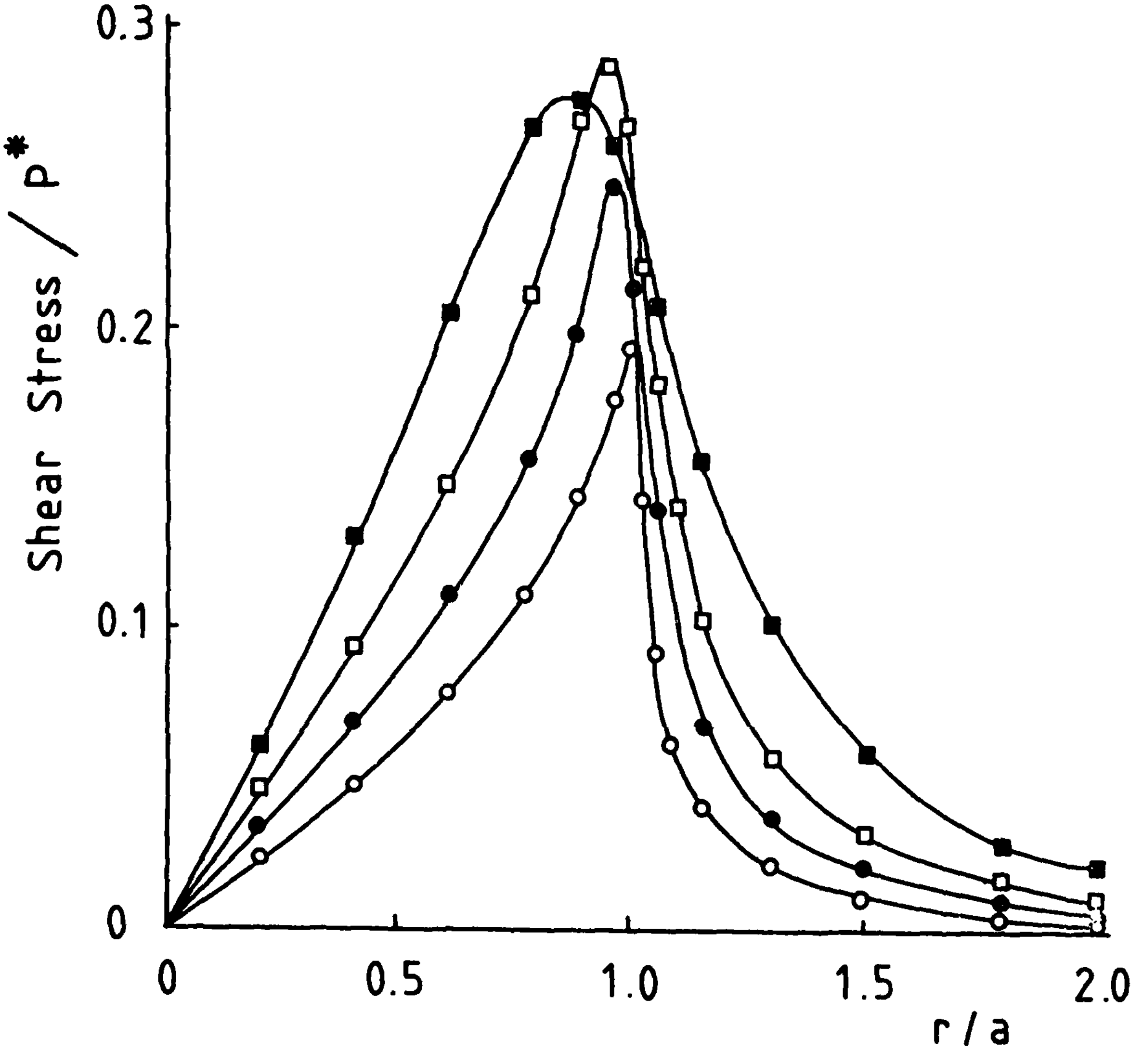

Figure 20. Variation of the radial shear stress as a function of the coating thickness ($E_c = 10\ E_s$ and $\nu_c = 0.20$ for all coatings).

○ : d = 0.025a ● : d = 0.05a

□ : d = 0.1a ■ : d = 0.2a

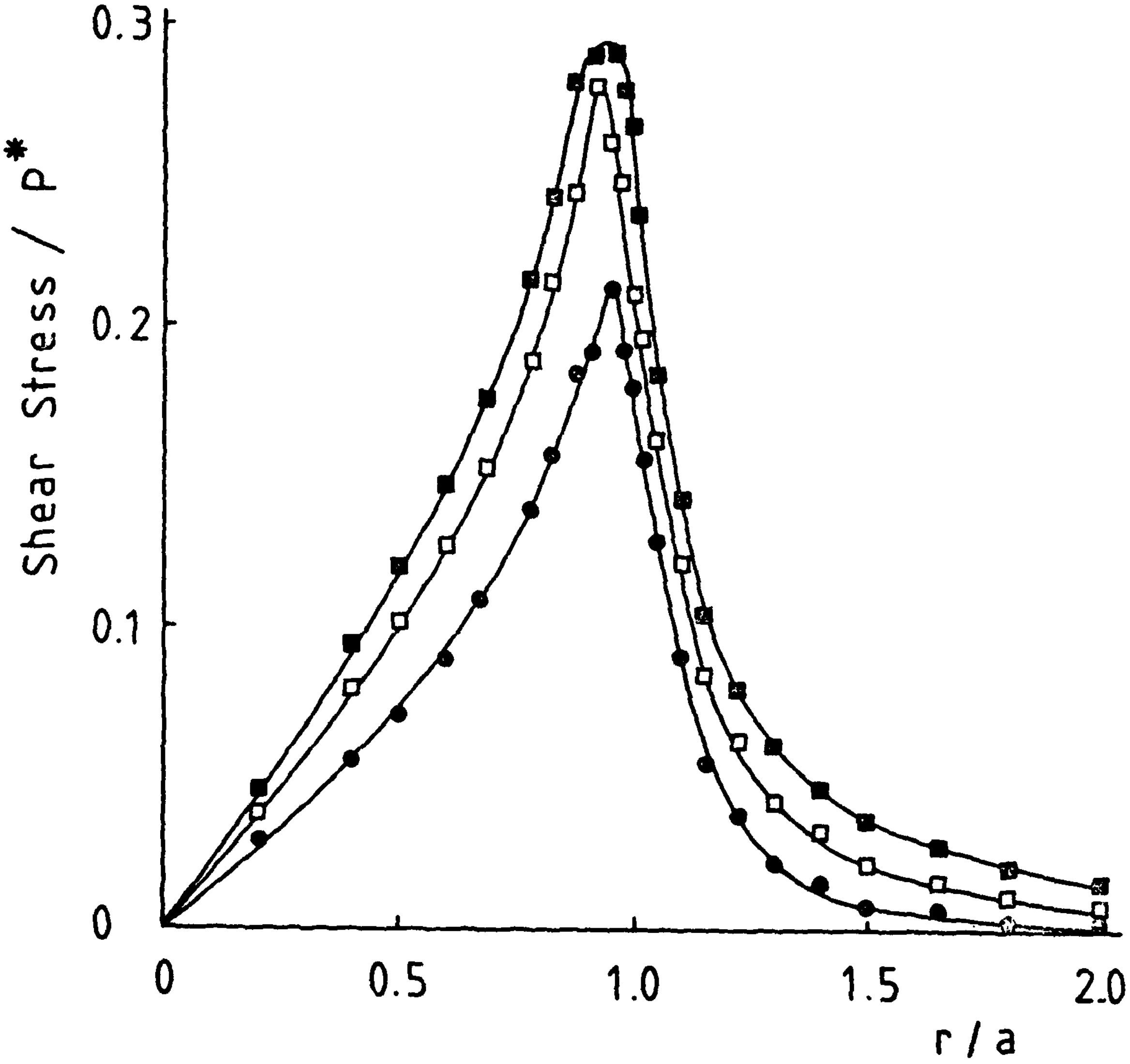

Figure 21. Variation of the radial shear stress as a function of Young's modulus of the coating (ν_c = 0.25 and d = 0.1a for all coatings).

● : E_c = 2 E_s; □ : E_c = 5 E_s ■ : E_c = 10 E_s

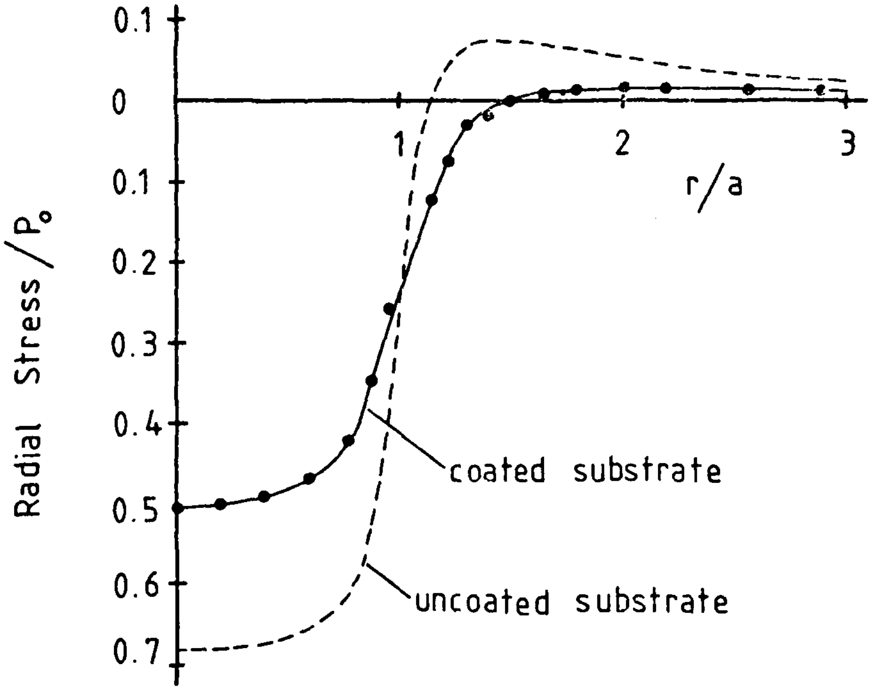

Figure 22. **Radial stress at the interface for a uniform pressure.**

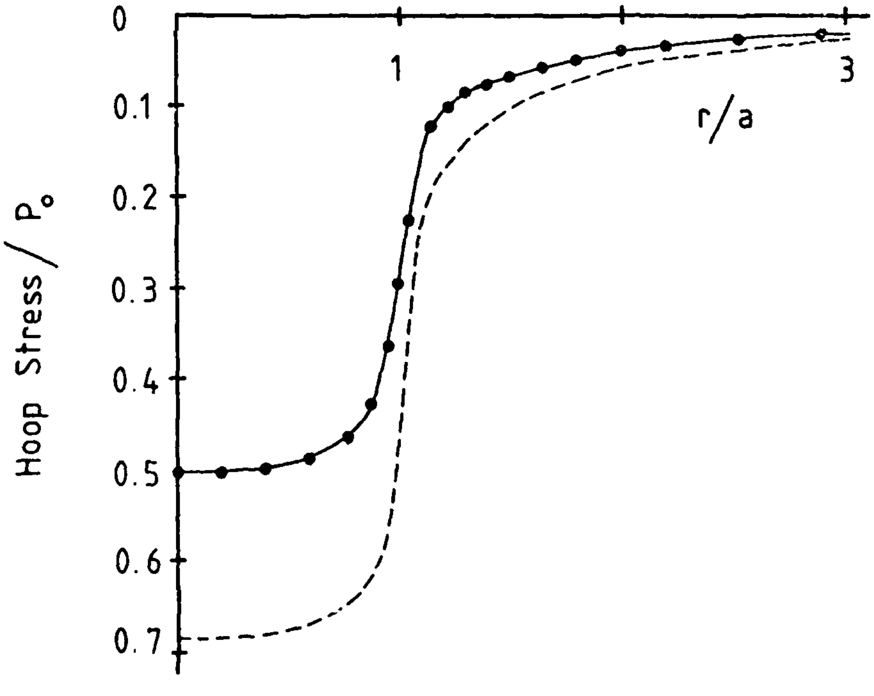

Figure 23. **Circumferential stress at the interface for a uniform pressure.**

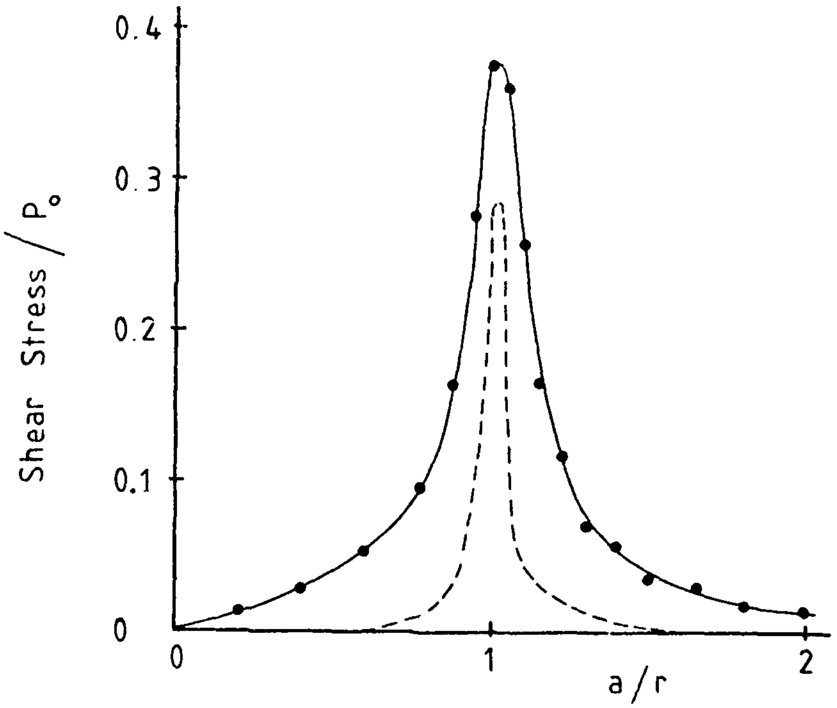

Figure 24. Interfacial shear stress for a uniform pressure.

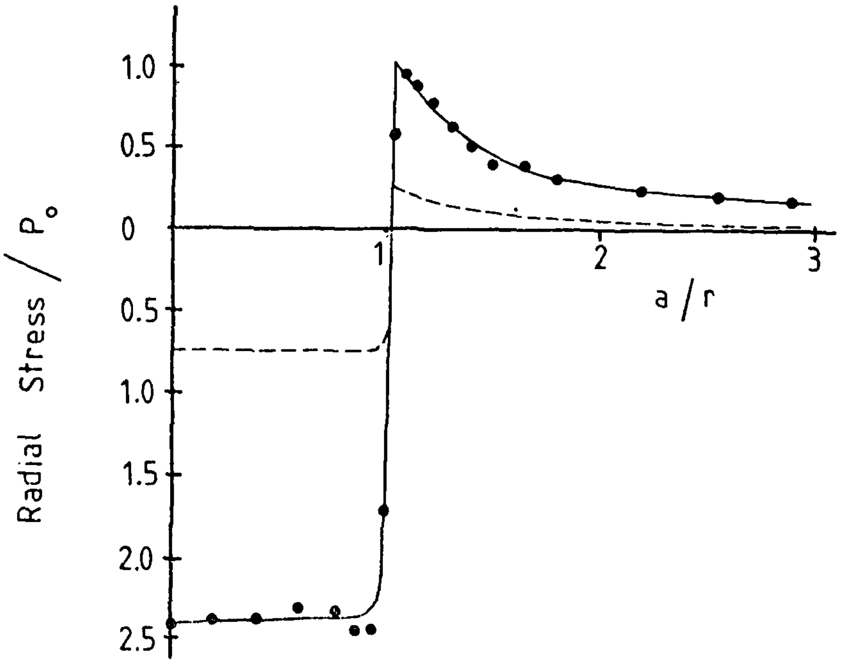

Figure 25. Radial stress at the surface for a uniform pressure. Dashed line indicates the radial stress for an uncoated substrate.

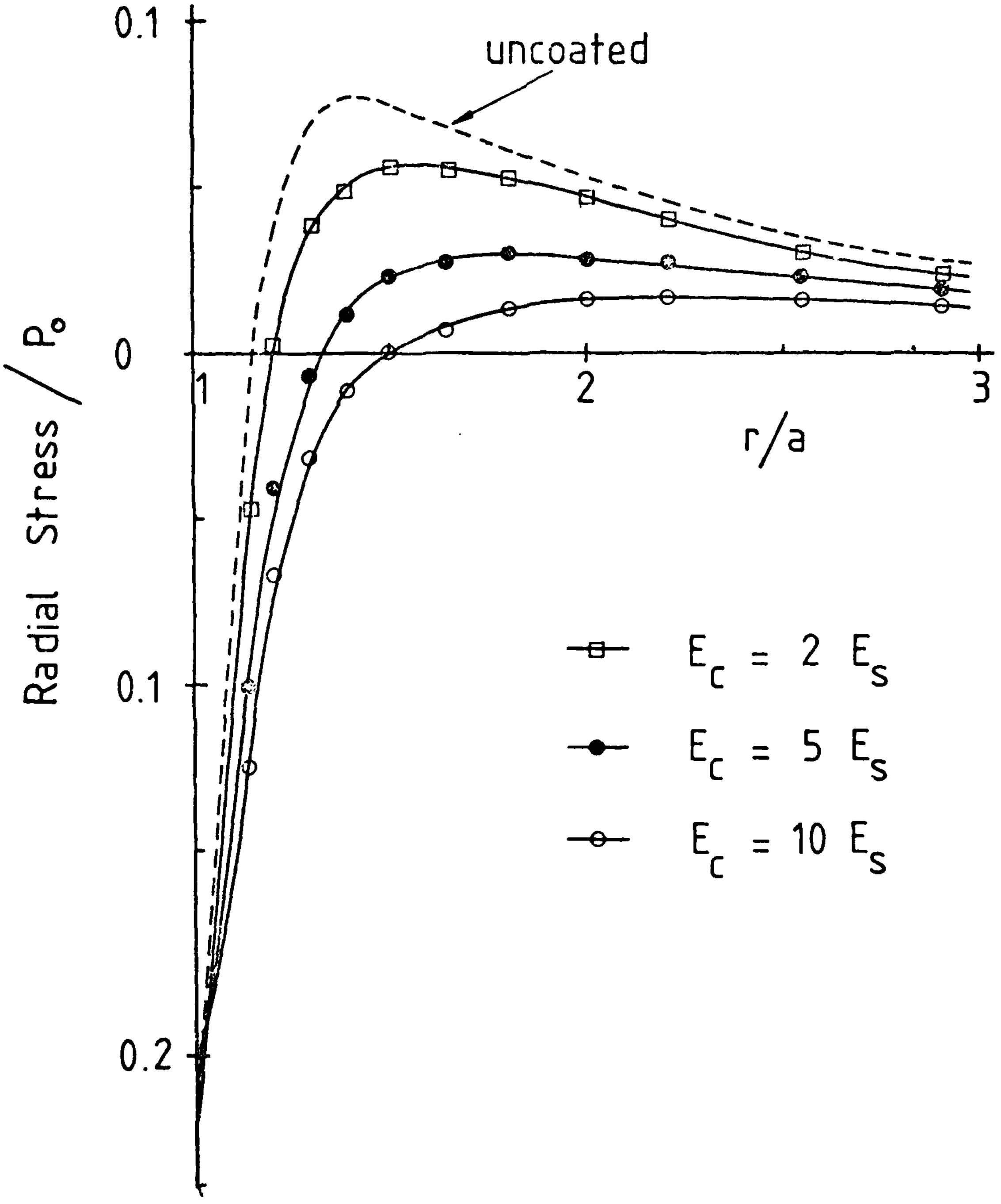

Figure 26. Radial stress at the interface and outside the contact area for three different Young's moduli of the coating material (see text).

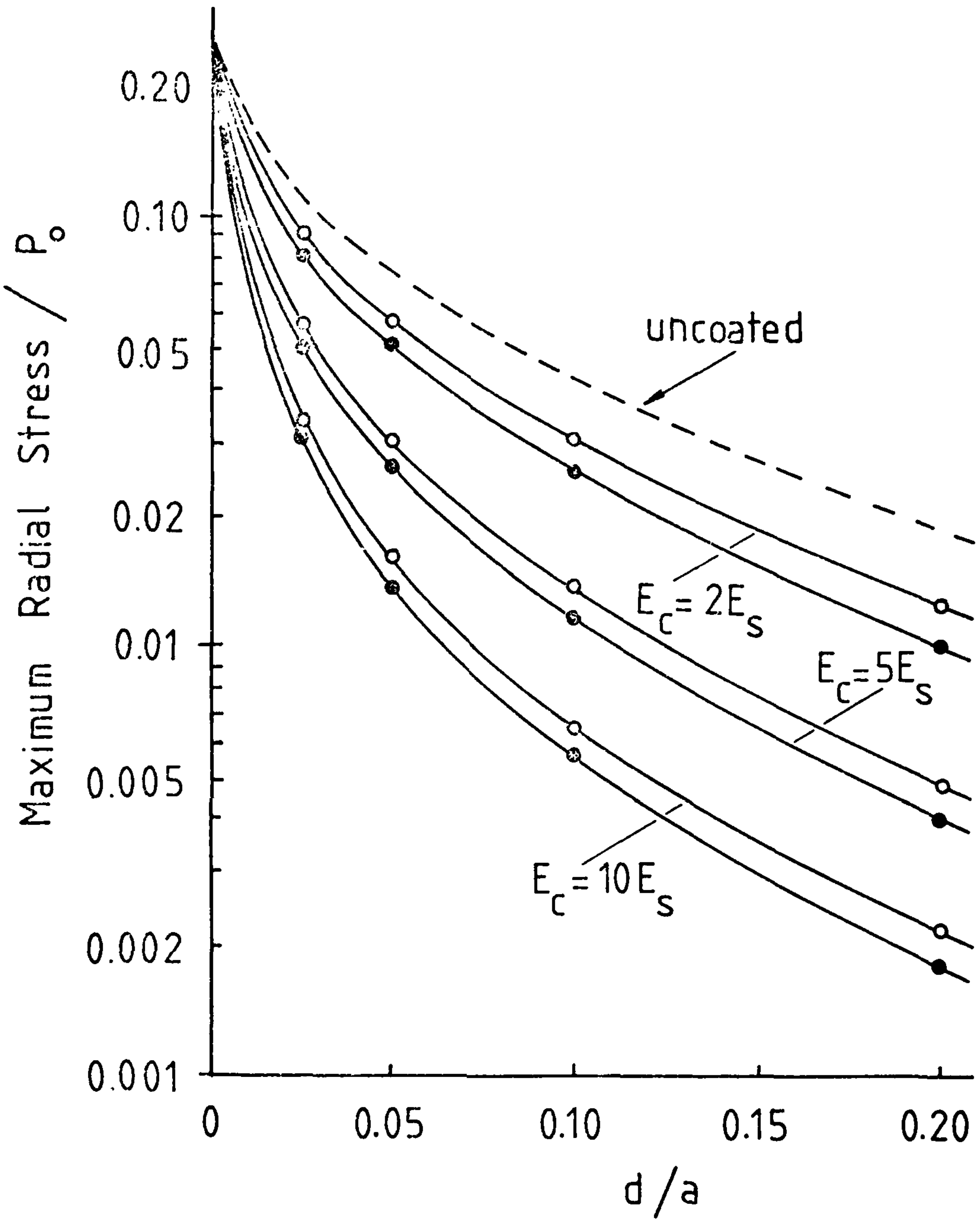

Figure 27. Effect of the coating parameters on the maximum radial stress at the interface for a uniform pressure

○ : $\nu_c = 0.20$ ● : $\nu_c = 0.30$

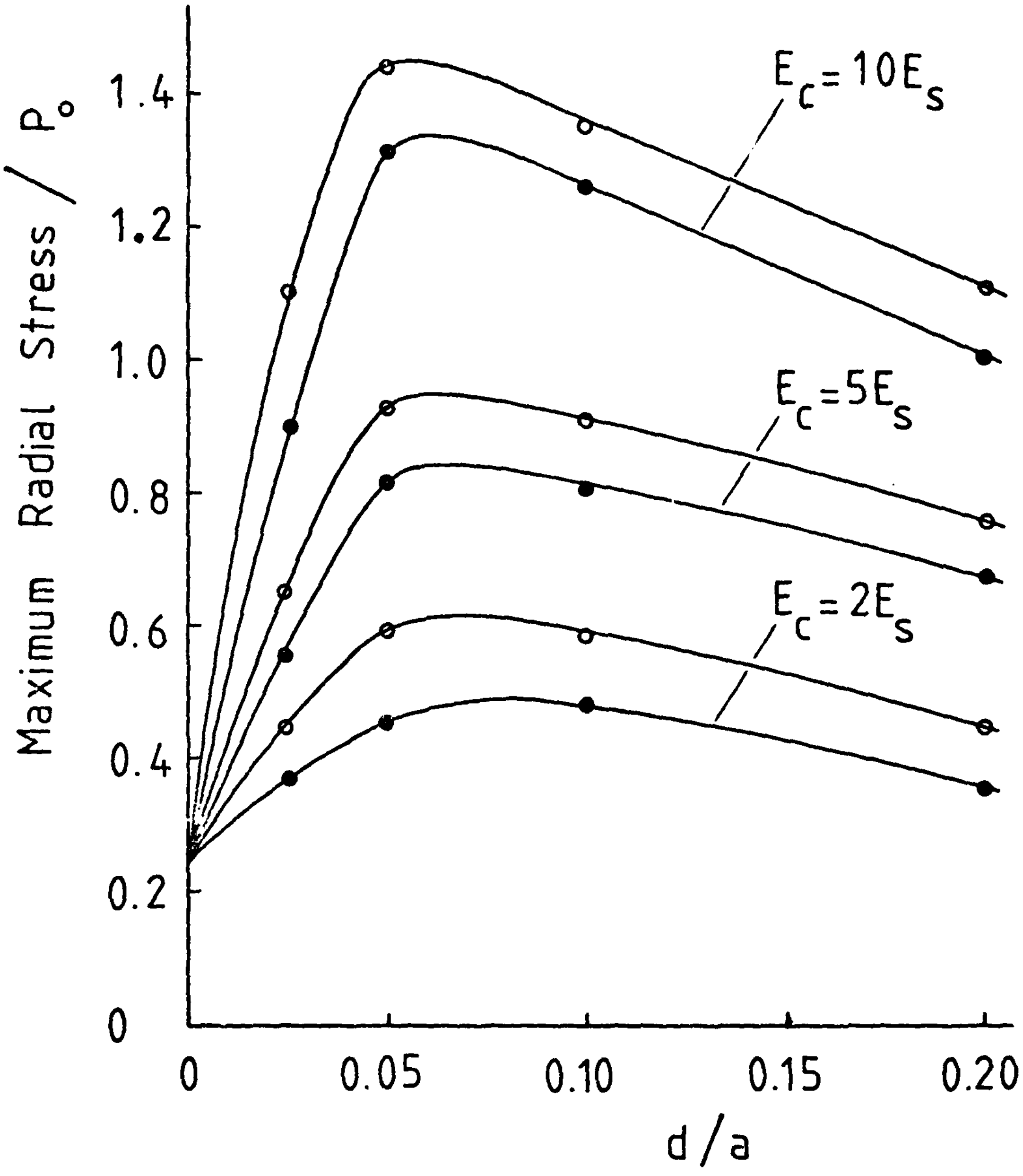

Figure 28. **Effect of the coating parameters on the maximum radial tensile stress at the coating surface.**

o : ν_c = 0.20 ● : ν_c = 0.30

29(a)

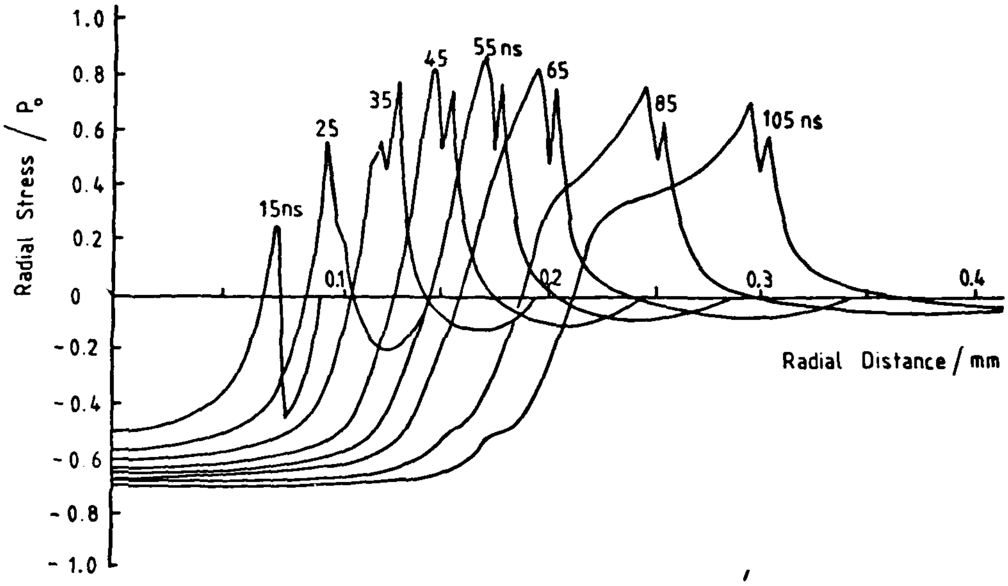

29(b)

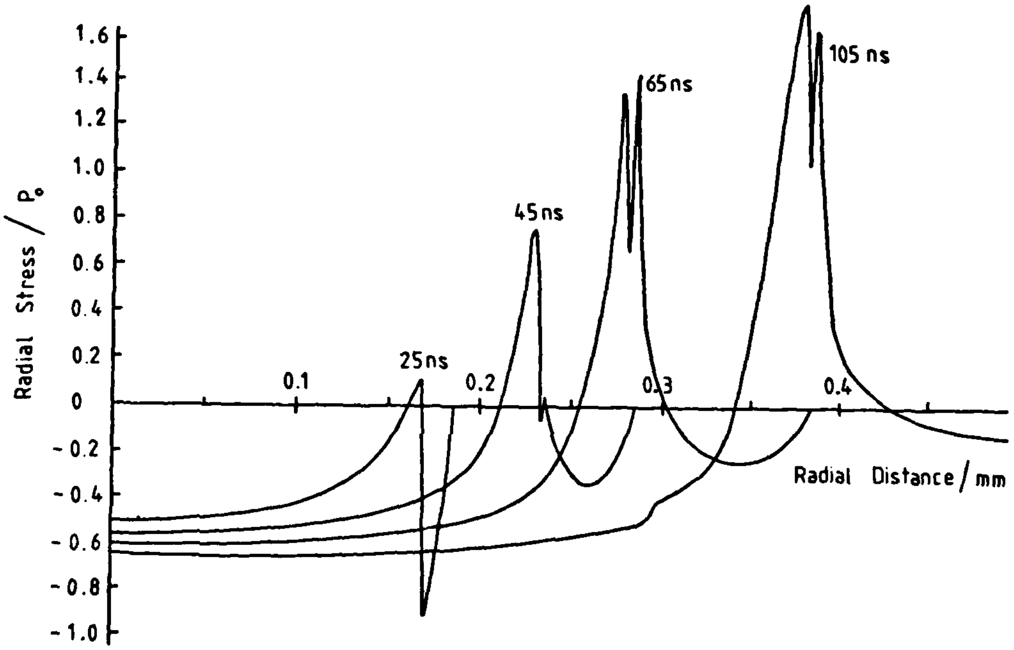

Figure 29. Development of the radial stress at the surface of uncoated zinc sulphide for an expanding uniform pressure

a) impact velocity 200 m s^{-1}

b) impact velocity 600 m s^{-1}

☆U.S.Government Printing Office: 1982 — 559-006/5080